

**Dynamics of the quasielastic  $^{16}\text{O}(e, e'p)$  reaction at  $Q^2 \approx 0.8$  (GeV/c) $^2$** 

K. G. Fissum,<sup>1,2,\*</sup> M. Liang,<sup>3</sup> B. D. Anderson,<sup>4</sup> K. A. Aniol,<sup>5</sup> L. Auerbach,<sup>6</sup> F. T. Baker,<sup>7</sup> J. Berthot,<sup>8</sup> W. Bertozzi,<sup>1</sup> P.-Y. Bertin,<sup>8</sup> L. Bimbot,<sup>9</sup> W. U. Boeglin,<sup>10</sup> E. J. Brash,<sup>11</sup> V. Breton,<sup>8</sup> H. Breuer,<sup>12</sup> E. Burtin,<sup>13</sup> J. R. Calarco,<sup>14</sup> L. S. Cardman,<sup>3</sup> G. D. Cates,<sup>15,16</sup> C. Cavata,<sup>13</sup> C. C. Chang,<sup>12</sup> J.-P. Chen,<sup>3</sup> E. Cisbani,<sup>17</sup> D. S. Dale,<sup>18</sup> C. W. de Jager,<sup>3</sup> R. De Leo,<sup>19</sup> A. Deur,<sup>8,16,3</sup> B. Diederich,<sup>20</sup> P. Djawotho,<sup>21</sup> J. Domingo,<sup>3</sup> J.-E. Ducret,<sup>13</sup> M. B. Epstein,<sup>22</sup> L. A. Ewell,<sup>12</sup> J. M. Finn,<sup>21</sup> H. Fonvieille,<sup>8</sup> B. Frois,<sup>13</sup> S. Frullani,<sup>17</sup> J. Gao,<sup>1,23</sup> F. Garibaldi,<sup>17</sup> A. Gasparian,<sup>18,24</sup> S. Gilad,<sup>1</sup> R. Gilman,<sup>3,25</sup> A. Glamazdin,<sup>26</sup> C. Glashauser,<sup>25</sup> J. Gomez,<sup>3</sup> V. Gorbenko,<sup>26</sup> T. Gorringer,<sup>18</sup> F. W. Hersman,<sup>14</sup> R. Holmes,<sup>27</sup> M. Holtrop,<sup>14</sup> N. d'Hose,<sup>13</sup> C. Howell,<sup>28</sup> G. M. Huber,<sup>11</sup> C. E. Hyde-Wright,<sup>20</sup> M. Iodice,<sup>17,29</sup> S. Jaminion,<sup>8</sup> M. K. Jones,<sup>21,3</sup> K. Joo,<sup>16,7</sup> C. Jutier,<sup>8,20</sup> W. Kahl,<sup>27</sup> S. Kato,<sup>30</sup> J. J. Kelly,<sup>12</sup> S. Kerhoas,<sup>13</sup> M. Khandaker,<sup>31</sup> M. Khayat,<sup>4</sup> K. Kino,<sup>32</sup> W. Korsch,<sup>18</sup> L. Kramer,<sup>10</sup> K. S. Kumar,<sup>15,33</sup> G. Kumbartzki,<sup>25</sup> G. Laveissière,<sup>8</sup> A. Leone,<sup>34</sup> J. J. LeRose,<sup>3</sup> L. Levchuk,<sup>26</sup> R. A. Lindgren,<sup>16</sup> N. Liyanage,<sup>1,3,16</sup> G. J. Lolos,<sup>11</sup> R. W. Lourie,<sup>35,36</sup> R. Madey,<sup>4,3,24</sup> K. Maeda,<sup>32</sup> S. Malov,<sup>25</sup> D. M. Manley,<sup>4</sup> D. J. Margaziotis,<sup>22</sup> P. Markowitz,<sup>10</sup> J. Martino,<sup>13</sup> J. S. McCarthy,<sup>16</sup> K. McCormick,<sup>20,4,25</sup> J. McIntyre,<sup>25</sup> R. L. J. van der Meer,<sup>11,3</sup> Z.-E. Meziani,<sup>6</sup> R. Michaels,<sup>3</sup> J. Mougey,<sup>37</sup> S. Nanda,<sup>3</sup> D. Neyret,<sup>13</sup> E. A. J. M. Offermann,<sup>3,36</sup> Z. Papandreou,<sup>11</sup> C. F. Perdrisat,<sup>21</sup> R. Perrino,<sup>34</sup> G. G. Petratos,<sup>4</sup> S. Platchkov,<sup>13</sup> R. Pomatsalyuk,<sup>26</sup> D. L. Prout,<sup>4</sup> V. A. Punjabi,<sup>31</sup> T. Pussieux,<sup>13</sup> G. Quémener,<sup>21,8,37</sup> R. D. Ransome,<sup>25</sup> O. Ravel,<sup>8</sup> Y. Roblin,<sup>8,3</sup> R. Roche,<sup>38,20</sup> D. Rowntree,<sup>1</sup> G. A. Rutledge,<sup>21,4</sup> P. M. Rutt,<sup>25</sup> A. Saha,<sup>3</sup> T. Saito,<sup>32</sup> A. J. Sarty,<sup>38,39</sup> A. Serdarevic-Offermann,<sup>11,3</sup> T. P. Smith,<sup>14</sup> A. Soldi,<sup>40</sup> P. Sorokin,<sup>26</sup> P. Souder,<sup>27</sup> R. Suleiman,<sup>4,1</sup> J. A. Templon,<sup>7,8</sup> T. Terasawa,<sup>32</sup> L. Todor,<sup>20,11</sup> H. Tsubota,<sup>32</sup> H. Ueno,<sup>30</sup> P. E. Ulmer,<sup>20</sup> G. M. Urciuoli,<sup>17</sup> P. Vernin,<sup>13</sup> S. van Verst,<sup>1</sup> B. Vlahovic,<sup>40,3</sup> H. Voskanyan,<sup>41</sup> J. W. Watson,<sup>4</sup> L. B. Weinstein,<sup>20</sup> K. Wijesooriya,<sup>21,42,28</sup> B. Wojtsekhowski,<sup>3</sup> D. G. Zainea,<sup>11</sup> V. Zeps,<sup>18</sup> J. Zhao,<sup>1</sup> and Z.-L. Zhou<sup>1</sup>

(Jefferson Lab Hall A Collaboration)

<sup>1</sup>Massachusetts Institute of Technology, Cambridge, Massachusetts 02139, USA<sup>2</sup>University of Lund, Box 118, SE-221 00 Lund, Sweden<sup>3</sup>Thomas Jefferson National Accelerator Facility, Newport News, Virginia 23606, USA<sup>4</sup>Kent State University, Kent, Ohio 44242, USA<sup>5</sup>California State University Los Angeles, Los Angeles, California 90032, USA<sup>6</sup>Temple University, Philadelphia, Pennsylvania 19122, USA<sup>7</sup>University of Georgia, Athens, Georgia 30602, USA<sup>8</sup>IN2P3, F-63177 Aubièrre, France<sup>9</sup>Institut de Physique Nucléaire, F-91406 Orsay, France<sup>10</sup>Florida International University, Miami, Florida 33199, USA<sup>11</sup>University of Regina, Regina, Saskatchewan, Canada, S4S 0A2<sup>12</sup>University of Maryland, College Park, Maryland 20742, USA<sup>13</sup>CEA Saclay, F-91191 Gif-sur-Yvette, France<sup>14</sup>University of New Hampshire, Durham, New Hampshire 03824, USA<sup>15</sup>Princeton University, Princeton, New Jersey 08544, USA<sup>16</sup>University of Virginia, Charlottesville, Virginia 22901, USA<sup>17</sup>INFN, Sezione Sanità and Istituto Superiore di Sanità, Laboratorio di Fisica, I-00161 Rome, Italy<sup>18</sup>University of Kentucky, Lexington, Kentucky 40506, USA<sup>19</sup>INFN, Sezione di Bari and University of Bari, I-70126 Bari, Italy<sup>20</sup>Old Dominion University, Norfolk, Virginia 23529, USA<sup>21</sup>College of William and Mary, Williamsburg, Virginia 23187, USA<sup>22</sup>California State University, Los Angeles, California 90032, USA<sup>23</sup>California Institute of Technology, Pasadena, California 91125, USA<sup>24</sup>Hampton University, Hampton, Virginia 23668, USA<sup>25</sup>Rutgers, The State University of New Jersey, Piscataway, New Jersey 08554, USA<sup>26</sup>Kharkov Institute of Physics and Technology, Kharkov 61108, Ukraine<sup>27</sup>Syracuse University, Syracuse, New York 13244, USA<sup>28</sup>Duke University, Durham, North Carolina 27706, USA<sup>29</sup>INFN, Sezione di Roma III, I-00146 Rome, Italy<sup>30</sup>Yamagata University, Yamagata 990, Japan<sup>31</sup>Norfolk State University, Norfolk, Virginia 23504 USA<sup>32</sup>Tohoku University, Sendai 980, Japan<sup>33</sup>University of Massachusetts, Amherst, Massachusetts 01003, USA<sup>34</sup>INFN, Sezione di Lecce, I-73100 Lecce, Italy<sup>35</sup>State University of New York at Stony Brook, Stony Brook, New York 11794, USA<sup>36</sup>Renaissance Technologies Corporation, Setauket, New York 11733, USA<sup>37</sup>Laboratoire de Physique Subatomique et de Cosmologie, F-38026 Grenoble, France<sup>38</sup>Florida State University, Tallahassee, Florida 32306, USA<sup>39</sup>Saint Mary's University, Halifax, Nova Scotia, Canada, B3H 3C3

<sup>40</sup>North Carolina Central University, Durham, North Carolina 27707, USA<sup>41</sup>Yerevan Physics Institute, Yerevan 375036, Armenia<sup>42</sup>Argonne National Lab, Argonne, Illinois 60439, USA

J. M. Udías and J. R. Vignote

Universidad Complutense de Madrid, E-28040 Madrid, Spain

J. Ryckebusch and D. Debruyne

Ghent University, B-9000 Ghent, Belgium

(Received 20 January 2004; published 20 September 2004)

The physics program in Hall A at Jefferson Lab commenced in the summer of 1997 with a detailed investigation of the  $^{16}\text{O}(e, e'p)$  reaction in quasielastic, constant  $(q, \omega)$  kinematics at  $Q^2 \approx 0.8$  (GeV/c) $^2$ ,  $q \approx 1$  GeV/c, and  $\omega \approx 445$  MeV. Use of a self-calibrating, self-normalizing, thin-film waterfall target enabled a systematically rigorous measurement. Five-fold differential cross-section data for the removal of protons from the  $1p$ -shell have been obtained for  $0 < p_{\text{miss}} < 350$  MeV/c. Six-fold differential cross-section data for  $0 < E_{\text{miss}} < 120$  MeV were obtained for  $0 < p_{\text{miss}} < 340$  MeV/c. These results have been used to extract the  $A_{LT}$  asymmetry and the  $R_L$ ,  $R_T$ ,  $R_{LT}$ , and  $R_{L+TT}$  effective response functions over a large range of  $E_{\text{miss}}$  and  $p_{\text{miss}}$ . Detailed comparisons of the  $1p$ -shell data with Relativistic Distorted-Wave Impulse Approximation (RDWIA), Relativistic Optical-Model Eikonal Approximation (ROMEIA), and Relativistic Multiple-Scattering Glauber Approximation (RMSGGA) calculations indicate that two-body currents stemming from meson-exchange currents (MEC) and isobar currents (IC) are not needed to explain the data at this  $Q^2$ . Further, dynamical relativistic effects are strongly indicated by the observed structure in  $A_{LT}$  at  $p_{\text{miss}} \approx 300$  MeV/c. For  $25 < E_{\text{miss}} < 50$  MeV and  $p_{\text{miss}} \approx 50$  MeV/c, proton knockout from the  $1s_{1/2}$ -state dominates, and ROMEIA calculations do an excellent job of explaining the data. However, as  $p_{\text{miss}}$  increases, the single-particle behavior of the reaction is increasingly hidden by more complicated processes, and for  $280 < p_{\text{miss}} < 340$  MeV/c, ROMEIA calculations together with two-body currents stemming from MEC and IC account for the shape and transverse nature of the data, but only about half the magnitude of the measured cross section. For  $50 < E_{\text{miss}} < 120$  MeV and  $145 < p_{\text{miss}} < 340$  MeV/c,  $(e, e'pN)$  calculations which include the contributions of central and tensor correlations (two-nucleon correlations) together with MEC and IC (two-nucleon currents) account for only about half of the measured cross section. The kinematic consistency of the  $1p$ -shell normalization factors extracted from these data with respect to all available  $^{16}\text{O}(e, e'p)$  data is also examined in detail. Finally, the  $Q^2$ -dependence of the normalization factors is discussed.

DOI: 10.1103/PhysRevC.70.034606

PACS number(s): 25.30.Fj, 24.70.+s, 27.20.+n

## I. INTRODUCTION

Exclusive and semi-exclusive  $(e, e'p)$  in quasielastic (QE) kinematics<sup>1</sup> has long been used as a precision

tool for the study of nuclear electromagnetic responses (see Refs. [1–4]). Cross-section data have provided information used to study the single-nucleon aspects of nuclear structure and the momentum distributions of protons bound inside the nucleus, as well as to search for non-nucleonic degrees of freedom and to stringently test nuclear theories. Effective response-function separations<sup>2</sup> have been used to extract detailed information about the different reaction mechanisms contributing to the cross section since they are selectively sensitive to different aspects of the nuclear current.

\*Corresponding author. Email address: kevin.fissum@nuclear.lu.se

<sup>†</sup>Present address: University of Connecticut, Storrs, Connecticut 06269, USA.

<sup>‡</sup>Present address: TRIUMF, Vancouver, British Columbia, Canada V6T 2A3.

<sup>§</sup>Present address: NIKHEF, Amsterdam, The Netherlands.

<sup>||</sup>Present address: Carnegie Mellon University, Pittsburgh, Pennsylvania 15217, USA.

<sup>1</sup>Kinematically, an electron scattered through an angle  $\theta_e$  transfers momentum  $\mathbf{q}$  and energy  $\omega$  with  $Q^2 = \mathbf{q}^2 - \omega^2$ . The ejected proton has mass  $m_p$ , momentum  $\mathbf{p}_p$ , energy  $E_p$ , and kinetic energy  $T_p$ . In QE kinematics,  $\omega \approx Q^2/2m_p$ . The cross section is typically measured as a function of missing energy  $E_{\text{miss}} = \omega - T_p - T_B$  and missing momentum  $p_{\text{miss}} = |\mathbf{q} - \mathbf{p}_p|$ .  $T_B$  is the kinetic energy of the residual nucleus. The lab polar angle between the ejected proton and virtual photon is  $\theta_{pq}$  and the azimuthal angle is  $\phi$ .  $\theta_{pq} > 0^\circ$  corresponds to  $\phi = 180^\circ$ ,  $\theta_p > \theta_q$ , and  $+p_{\text{miss}}$ .  $\theta_{pq} < 0^\circ$  corresponds to  $\phi = 0^\circ$ ,  $\theta_p < \theta_q$ , and  $-p_{\text{miss}}$ .

Some of the first  $(e, e'p)$  energy- and momentum-distribution measurements were made by Amaldi *et al.* [5]. These results, and those which followed (see Refs. [1,2,6]), were interpreted within the framework of single-particle knockout from nuclear valence states, even though the measured cross-section data was as much as 40% lower than predicted by the models of the time. The first relativistic calculations for  $(e, e'p)$  bound-state proton knockout were

<sup>2</sup>In the One-Photon Exchange Approximation (OPEA), the unpolarized  $(e, e'p)$  cross section can be expressed as the sum of four independent response functions:  $R_L$  (longitudinal),  $R_T$  (transverse),  $R_{LT}$  (longitudinal-transverse interference), and  $R_{TT}$  (transverse-transverse interference). See also Eq. (4).

performed by Picklesimer, Van Orden, and Wallace [7–9]. Such Relativistic Distorted-Wave Impulse Approximation (RDWIA) calculations are generally expected to be more accurate at higher  $Q^2$ , since QE ( $e, e'p$ ) is expected to be dominated by single-particle interactions in this regime of four-momentum transfer.

Other aspects of the structure as well as of the reaction mechanism have generally been studied at higher missing energy ( $E_{\text{miss}}$ ). While it is experimentally convenient to perform measurements spanning the valence-state knockout and higher  $E_{\text{miss}}$  excitation regions simultaneously, there is as of yet no rigorous, coherent theoretical picture that uniformly explains the data for all  $E_{\text{miss}}$  and all missing momentum ( $p_{\text{miss}}$ ). In the past, the theoretical tools used to describe the two energy regimes have been somewhat different. Mütter and Dickhoff [10] suggest that the regions are related mainly by the transfer of strength from the valence states to higher  $E_{\text{miss}}$ .

The nucleus  $^{16}\text{O}$  has long been a favorite of theorists, since it has a doubly closed shell whose structure is thus easier to model than other nuclei. It is also a convenient target for experimentalists. While the knockout of  $1p$ -shell protons from  $^{16}\text{O}$  has been studied extensively in the past at lower  $Q^2$ , few data were available at higher  $E_{\text{miss}}$  and no data were available at higher  $Q^2$  when this experiment was conceived in 1989.

### A. $1p$ -shell knockout

The knockout of  $1p$ -shell protons in  $^{16}\text{O}(e, e'p)$  was studied by Bernheim *et al.* [11] and Chinitz *et al.* [12] at Saclay, Spaltro *et al.* [13] and Leuschner *et al.* [14] at NIKHEF, and Blomqvist *et al.* [15] at Mainz at  $Q^2 < 0.4$  (GeV/c) $^2$ . In these experiments, cross-section data for the lowest-lying fragments of each shell were measured as a function of  $p_{\text{miss}}$ , and normalization factors (relating how much lower the measured cross-section data were than predicted) were extracted. These published normalization factors ranged between 0.5 and 0.7, but Kelly [2,4] has since demonstrated that the Mainz data suggest a significantly smaller normalization factor (see also Table X).

Several calculations exist (see Refs. [16–21]) which demonstrate the sensitivity<sup>3</sup> of the longitudinal-transverse interference response function  $R_{LT}$  and the corresponding left-

<sup>3</sup>In the nonrelativistic Plane-Wave Impulse Approximation (PWIA), the transverse amplitude in the  $R_{LT}$  response is uniquely determined by the convection current. At higher  $Q^2$ , it is well-known that the convection current yields small matrix elements. As a result, the nonrelativistic Impulse Approximation (IA) contributions which dominate  $R_L$  and  $R_T$  are suppressed in  $R_{LT}$  (and thus  $A_{LT}$ ). Hence, these observables are particularly sensitive to any mechanisms beyond the IA, such as channel coupling and relativistic and two-body current mechanisms [89].

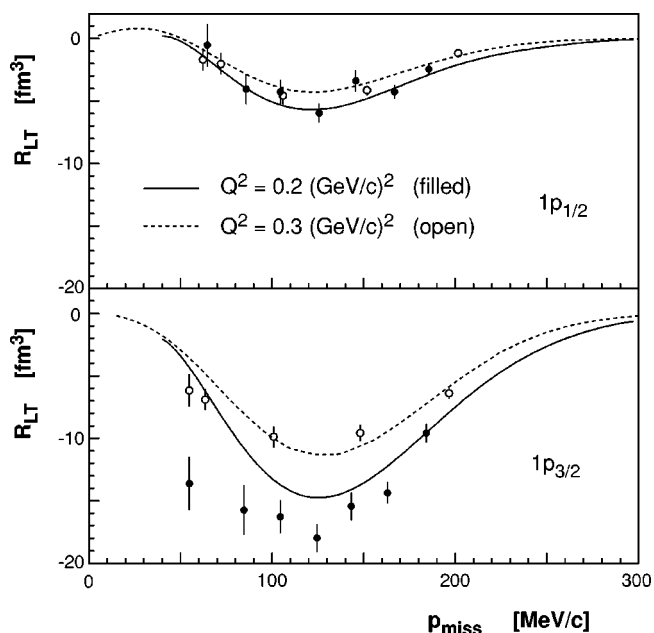


FIG. 1. Longitudinal-transverse interference effective responses  $R_{LT}$  as a function of  $p_{\text{miss}}$  for the removal of protons from the  $1p$ -shell of  $^{16}\text{O}$ . The open and filled circles were extracted from QE data obtained by Chinitz *et al.* at  $Q^2=0.3$  (GeV/c) $^2$  and Spaltro *et al.* at  $Q^2=0.2$  (GeV/c) $^2$ , respectively. The dashed [ $Q^2=0.3$  (GeV/c) $^2$ ] and solid [ $Q^2=0.2$  (GeV/c) $^2$ ] curves are modern RDWIA calculations. Overall, agreement is good, and improves with increasing  $Q^2$ .

right asymmetry  $A_{LT}$ <sup>4</sup> to “spinor distortion” (see Appendix A 1), especially for the removal of bound-state protons. Such calculations predict that proper inclusion of these dynamical relativistic effects is needed to simultaneously reproduce the cross-section data,  $A_{LT}$ , and  $R_{LT}$ .

Figure 1 shows the effective response  $R_{LT}$  as a function of  $p_{\text{miss}}$  for the removal of protons from the  $1p$ -shell of  $^{16}\text{O}$  for the QE data obtained by Chinitz *et al.* at  $Q^2=0.3$  (GeV/c) $^2$  (open circles) and Spaltro *et al.* at  $Q^2=0.2$  (GeV/c) $^2$  (solid circles) together with modern RDWIA calculations (see Secs. IV and V for a complete discussion of the calculations). The solid lines correspond to the  $0.2$  (GeV/c) $^2$  data, while the dashed lines correspond to the  $Q^2=0.3$  (GeV/c) $^2$  data. Overall, agreement is good, and as anticipated, improves with increasing  $Q^2$ .

### B. Higher missing energies

Few data are available for  $^{16}\text{O}(e, e'p)$  at higher  $E_{\text{miss}}$ , and much of what is known about this excitation region is from

<sup>4</sup> $A_{LT} \equiv [\sigma(\phi=0^\circ) - \sigma(\phi=180^\circ)] / [\sigma(\phi=0^\circ) + \sigma(\phi=180^\circ)]$ .  $A_{LT}$  is a particularly useful quantity for experimentalists because it is systematically much less challenging to extract than either an absolute cross section or an effective response function.

studies of other nuclei such as  $^{12}\text{C}$ . At MIT-Bates, a series of  $^{12}\text{C}(e, e'p)$  experiments have been performed at missing energies above the two-nucleon emission threshold (see Refs. [22–26]). The resulting cross-section data were much larger than the predictions of single-particle knockout models.<sup>5</sup> In particular, Ulmer *et al.* [23] identified a marked increase in the transverse-longitudinal difference  $S_T - S_L$ .<sup>6</sup> A similar increase has subsequently been observed by Lanen *et al.* for  $^6\text{Li}$  [27], by van der Steenhoven *et al.* for  $^{12}\text{C}$  [28], and most recently by Dutta *et al.* for  $^{12}\text{C}$  [29],  $^{56}\text{Fe}$ , and  $^{197}\text{Au}$  [30]. The transverse increase exists over a large range of four-momentum transfers, though the excess at lower  $p_{\text{miss}}$  seems to decrease with increasing  $Q^2$ . Theoretical attempts by Takaki [31], the Ghent Group [32], and Gil *et al.* [33] to explain the data at high  $E_{\text{miss}}$  using two-body knockout models coupled to Final-State Interactions (FSI) have not succeeded. Even for QE kinematics, this transverse increase which starts at the two-nucleon knockout threshold seems to be a strong signature of multinucleon currents.

## II. EXPERIMENT

This experiment [34,35], first proposed by Bertozzi *et al.* in 1989, was the inaugural physics investigation performed in Hall A [36] (the High Resolution Spectrometer Hall) at the Thomas Jefferson National Accelerator Facility (JLab) [37]. An overview of the apparatus in the Hall at the time of this measurement is shown in Fig. 2. For a thorough discussion of the experimental infrastructure and its capabilities, the interested reader is directed to the paper by Alcorn *et al.* [38]. For the sake of completeness, a subset of the aforementioned information is presented here.

### A. Electron beam

Unpolarized 70  $\mu\text{A}$  continuous electron beams with energies of 0.843, 1.643, and 2.442 GeV (corresponding to the virtual photon polarizations shown in Table I) were used for this experiment. A subsequent analysis of the data demonstrated that the actual beam energies were within 0.3% of the nominal values [39]. The typical laboratory  $\pm 4\sigma$  beam envelope at the target was 0.5 mm (horizontal) by 0.1 mm (vertical). Beam-current monitors [40] (calibrated using an Unser monitor [41]) were used to determine the total charge deliv-

<sup>5</sup> $1s$ -shell nucleons are generally knocked out from high-density regions of the target nucleus. In these high-density regions, the IA is expected to be less valid than for knockout from the valence  $1p$ -shell states lying near the surface. In this region of “less-valid” IA, sizeable contributions to the  $1s$ -shell cross-section data arise from two-nucleon current contributions stemming from meson-exchange currents (MEC) and isobar currents (IC). In addition to affecting the single-nucleon knockout cross section, the two-nucleon currents can result in substantial multi-nucleon knockout contributions to the higher  $E_{\text{miss}}$  continuum cross section [89].

<sup>6</sup>The transverse-longitudinal difference is  $S_T - S_L$ , where  $S_X = \sigma_{\text{Mott}} v_X R_X / \sigma_{ep}^X$ , and  $X \in \{T, L\}$ .  $\sigma_{ep}^X$  represents components of the off-shell  $ep$  cross section and may be calculated using the CC1, CC2, or CC3 prescriptions of de Forest [117].

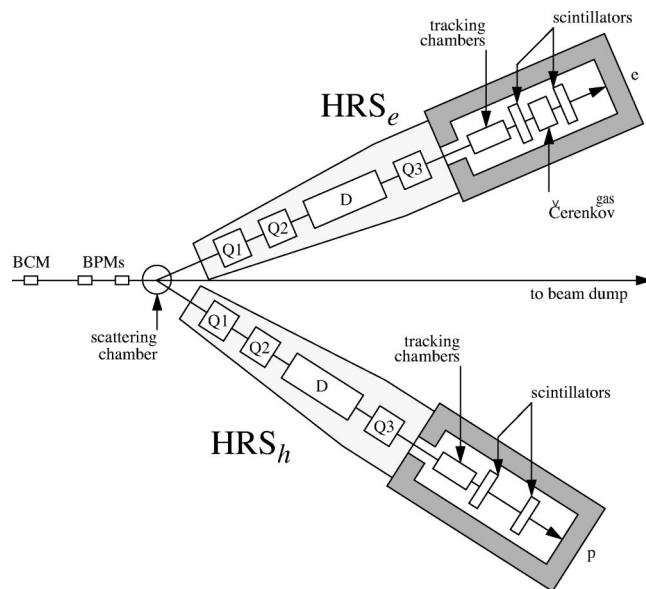


FIG. 2. The experimental infrastructure in Hall A at Jefferson Lab at the time of this experiment. The electron beam passed through a beam-current monitor (BCM) and beam-position monitors (BPMs) before striking a waterfall target located in the scattering chamber. Scattered electrons were detected in the  $\text{HRS}_e$ , while knocked-out protons were detected in the  $\text{HRS}_h$ . Noninteracting electrons were dumped. The spectrometers could be rotated about the central pivot.

ered to the target to an accuracy of 2% [42]. Beam-position monitors (BPMs) [43,44] were used to ensure that the location of the beam at the target was no more than 0.2 mm from the beamline axis, and that the instantaneous angle between the beam and the beamline axis was no larger than 0.15 mrad. The readout from the BCM and BPMs was continuously passed into the data stream [45]. Noninteracting electrons were dumped in a well-shielded, high-power beam dump [46] located roughly 30 m from the target.

### B. Target

A waterfall target [47] positioned inside a scattering chamber located at the center of the Hall provided the  $\text{H}_2\text{O}$  used for this study of  $^{16}\text{O}$ . The target canister was a rectangular box 20 cm long  $\times$  15 cm wide  $\times$  10 cm high containing air at atmospheric pressure. The beam entrance and exit windows to this canister were, respectively, 50  $\mu\text{m}$  and 75  $\mu\text{m}$  gold-plated beryllium foils. Inside the canister, three

TABLE I. The QE, constant ( $q, \omega$ ) kinematics employed in this measurement. At each beam energy,  $q \approx 1 \text{ GeV}/c$ ,  $\omega \approx 445 \text{ MeV}$ , and  $Q^2 \approx 0.8 (\text{GeV}/c)^2$ .

$E_{\text{beam}}$ (GeV)	$\theta_e$ ( $^\circ$ )	Virtual photon polarization	$\theta_{pq}$ ( $^\circ$ )
0.843	100.76	0.21	0, 8, 16
1.643	37.17	0.78	0, $\pm 8$
2.442	23.36	0.90	0, $\pm 2.5$ , $\pm 8$ , $\pm 16$ , $\pm 20$



TABLE II. Selected results from the optics commissioning.

Parameter	Resolution (FWHM)	Reconstruction accuracy
Out-of-plane angle	6.00 mrad	$\pm 0.60$ mrad
In-plane angle	2.30 mrad	$\pm 0.23$ mrad
$y_{\text{target}}$	2.00 mm	0.20 mm
$\Delta p/p$	$2.5 \times 10^{-4}$	

thin, parallel, flowing water films served as targets. This three-film configuration was superior to a single film  $3\times$  thicker because it reduced the target-associated multiple scattering and energy loss for particles originating in the first two films and it allowed for the determination of the film in which the scattering vertex was located, thereby facilitating a better overall correction for energy loss. The films were defined by  $2\text{ mm}\times 2\text{ mm}$  stainless-steel posts. Each film was separated by 25 mm along the direction of the beam, and was rotated beam right such that the normal to the film surface made an angle of  $30^\circ$  with respect to the beam direction. This geometry ensured that particles originating from any given film would not intersect any other film on their way into the spectrometers.

The thickness of the films could be changed by varying the speed of the water flow through the target loop via a pump. The average film thicknesses were fixed at  $(130\pm 2.5\%) \text{ mg/cm}^2$  along the direction of the beam throughout the experiment, which provided a good trade-off between resolution and target thickness. The thickness of the central water film was determined by comparing  $^{16}\text{O}(e, e')$  cross-section data measured at  $q\approx 330\text{ MeV}/c$  obtained from both the film and a  $(155\pm 1.5\%) \text{ mg/cm}^2$  BeO target foil placed in a solid-target ladder mounted beneath the target canister. The thicknesses of the side films were determined by comparing the concurrently measured  $^1\text{H}(e, e)$  cross section obtained from these side films to that obtained from the central film. Instantaneous variations in the target-film thicknesses were monitored throughout the entire experiment by continuously measuring the  $^1\text{H}(e, e)$  cross section.

### C. Spectrometers and detectors

The base apparatus used in the experiment was a pair of optically identical 4 GeV/c superconducting High Resolution Spectrometers (HRS) [48]. These spectrometers have a nominal 9% momentum bite and a FWHM momentum resolution  $\Delta p/p$  of roughly  $10^{-4}$ . The nominal laboratory angular acceptance is  $\pm 25$  mrad (horizontal) by  $\pm 50$  mrad (vertical). Scattered electrons were detected in the Electron Spectrometer ( $\text{HRS}_e$ ), and knocked-out protons were detected in the Hadron Spectrometer ( $\text{HRS}_h$ ) (see Fig. 2). Before the experiment, the absolute momentum calibration of the spectrometers was determined to  $\Delta p/p=1.5\times 10^{-3}$  [39]. Before and during the experiment, both the optical properties and acceptances of the spectrometers were studied [49]. Some optical parameters are presented in Table II. During the experiment, the locations of the spectrometers were surveyed to an accu-

racy of 0.3 mrad at every angular location [50]. The status of the magnets was continuously monitored and logged [45].

The detector packages were located in well-shielded detector huts built on decks located above each spectrometer (approximately 25 m from the target and 15 m above the floor of the Hall). The bulk of the instrumentation electronics was also located in these huts, and operated remotely from the Counting House. The  $\text{HRS}_e$  detector package consisted of a pair of thin scintillator planes [51] used to create triggers, a Vertical Drift Chamber (VDC) package [52,53] used for particle tracking, and a Gas Čerenkov counter [54] used to distinguish between  $\pi^-$  and electron events. Identical elements, except for the Gas Čerenkov counter, were also present in the  $\text{HRS}_h$  detector package. The status of the various detector subsystems was continuously monitored and logged [45]. The individual operating efficiencies of each of these three devices was  $>99\%$ .

### D. Electronics and data acquisition

For a given spectrometer, a coincidence between signals from the two trigger-scintillator planes indicated a “single-arm” event. Simultaneous  $\text{HRS}_e$  and  $\text{HRS}_h$  singles events were recorded as “coincidence” events. The basic trigger logic [55] allowed a prescaled fraction of single-arm events to be written to the data stream. Enough  $\text{HRS}_e$  singles were taken for a 1% statistics  $^1\text{H}(e, e)$  cross-section measurement at each kinematics. Each spectrometer had its own VME crate (for scalers) and FASTBUS crate (for ADCs and TDCs). The crates were managed by readout controllers (ROCs). In addition to overseeing the state of the run, a trigger supervisor (TS) generated the triggers which caused the ROCs to read out the crates on an event-by-event basis. The VME (scaler) crate was also read out every ten seconds. An event builder (EB) collected the resulting data shards into events. An analyzer/data distributor (ANA/DD) analyzed and/or sent these events to the disk of the data-acquisition computer. The entire data-acquisition system was managed using the software toolkit CODA [56].

Typical scaler events were about 0.5 kb in length. Typical single-arm events were also about 0.5 kb, while typical coincidence events were about 1.0 kb. The acquisition deadtime was monitored by measuring the TS output-to-input ratio for each event type. The event rates were set by varying the prescale factors and the beam current such that the DAQ computer was busy at most only 20% of the time. This resulted in a relatively low event rate (a few kHz), at which the electronics deadtime was  $<1\%$ . Online analyzers [57] were used to monitor the quality of the data as it was taken. Eventually, the data were transferred to magnetic tape. The ultimate data analysis was performed on the DEC-8400 CPU farm ABACUS [58] at the Massachusetts Institute of Technology using the analysis package ESPACE [59].

## III. ANALYSIS

The interested reader is directed to the Ph.D. theses of Gao [60] and Liyanage [61] for a complete discussion of the

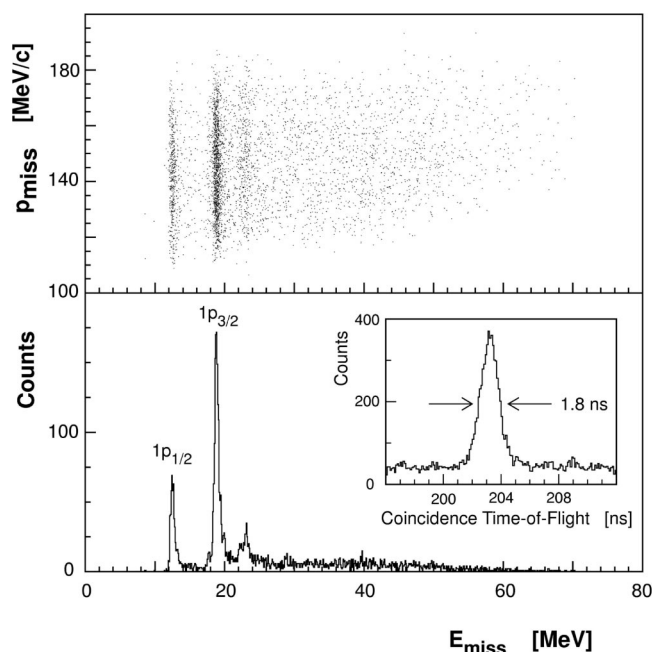


FIG. 3. Yield spectrum obtained at  $E_{\text{beam}}=0.843$  GeV and  $\theta_{pq}=+8^\circ$ , corresponding to  $p_{\text{miss}}=148$  MeV/ $c$ . Pion rejection has been performed, and all timing corrections have been applied. The top panel shows a scatterplot of  $p_{\text{miss}}$  versus  $E_{\text{miss}}$ . The dark vertical bands project into the peaks located at 12.1 and 18.3 MeV in the bottom panel. These peaks correspond to protons knocked-out of the  $1p_{1/2}$ - and  $1p_{3/2}$ -states of  $^{16}\text{O}$ , respectively. The  $E_{\text{miss}}$  resolution was roughly 0.9 MeV FWHM, which did not allow for separation of the  $2s_{1/2}1d_{5/2}$ -doublet located at  $E_{\text{miss}}=17.4$  MeV from the  $1p_{3/2}$ -state at 18.3 MeV. The bump located at roughly 23 MeV is a negative-parity doublet which was not investigated. The insert shows the corresponding optimized coincidence TOF peak which has a FWHM of 1.8 ns. The signal-to-noise ratio was about 8:1 in these kinematics.

data analysis. For the sake of completeness, a subset of the aforementioned information is presented here.

#### A. Timing corrections and particle identification

The identification of coincidence ( $e, e'p$ ) events was in general a straightforward process. Software corrections were applied to remove timing variations induced by the trigger-scintillator circuit and thus sharpen all flight-time peaks. These included corrections to proton flight times due to variations in the proton kinetic energies, and corrections for variations in the electron and proton path lengths through the spectrometers. Pion rejection was performed using a flight-time cut for  $\pi^+$ s in the  $\text{HRS}_h$  and the Gas Čerenkov for  $\pi^-$ s in the  $\text{HRS}_e$ . A sharp, clear, coincidence Time-of-Flight (TOF) peak with a FWHM of 1.8 ns resulted (see Fig. 3). High-energy correlated protons which punched through the  $\text{HRS}_h$  collimator ( $<10\%$  of the prompt yield) were rejected by requiring both spectrometers to independently reconstruct the coincidence-event vertex in the vicinity of the same water film. The resulting prompt-peak yields for each water film were corrected for uncorrelated (random) events present in the peak-time region on a bin-by-bin basis as per the method

suggested by Owens [62]. These per-film yields were then normalized individually.

#### B. Normalization

The relative focal-plane efficiencies for each of the two spectrometers were measured independently for each of the three water films at every spectrometer excitation used in the experiment. By measuring the same single-arm cross section at different locations on the spectrometer focal planes, variations in the relative efficiencies were identified. The position variation across the focal plane was investigated by systematically shifting the central excitation of the spectrometer about the mean momentum setting in a series of discrete steps such that the full momentum acceptance was “mapped”. A smooth, slowly varying dip-region cross section was used instead of a single discrete peak for continuous coverage of the focal plane. The relative-efficiency profiles were unfolded from these data using the program RELEFF [63] by Baghaei. For each water film, solid-angle cuts were then applied to select the “flat” regions of the angular acceptance. These cuts reduced the spectrometer apertures by roughly 20% to about 4.8 msr. Finally, relative-momentum cuts were applied to select the flat regions of momentum acceptance. These cuts reduced the spectrometer momentum acceptance by roughly 22% to  $-3.7\% < \delta < 3.3\%$ . The resulting acceptance profile of each spectrometer was uniform to within 1%.

The absolute efficiency at which the two spectrometers operated in coincidence mode was given by

$$\epsilon = \epsilon_e \cdot \epsilon_p \cdot \epsilon_{\text{coin}}, \quad (1)$$

where  $\epsilon_e$  was the single-arm  $\text{HRS}_e$  efficiency,  $\epsilon_p$  was the single-arm  $\text{HRS}_h$  efficiency, and  $\epsilon_{\text{coin}}$  was the coincidence-trigger efficiency. The quantity  $(\epsilon_p \cdot \epsilon_{\text{coin}})$  was measured at  $\theta_{pq}=0^\circ$  and  $E_{\text{beam}}=0.843$  GeV using the  $^1\text{H}(e, e)$  reaction. A 0.7 msr collimator was placed in front of the  $\text{HRS}_e$ . In these kinematics, the cone of recoil protons fit entirely into the central flat-acceptance region of the  $\text{HRS}_h$ . The number of  $^1\text{H}(e, e)$  events where the proton was also detected was compared to the number of  $^1\text{H}(e, e)$  events where the proton was not detected to yield a product of efficiencies  $(\epsilon_p \cdot \epsilon_{\text{coin}})$  of 98.9%. The 1.1% effect was due to proton absorption in the waterfall target exit windows, spectrometer windows, and the first layer of trigger scintillators. Since the central field of the  $\text{HRS}_h$  was held constant throughout the entire experiment, this measurement was applicable to each of the hadron kinematics employed. A similar method was used to determine the quantity  $(\epsilon_e \cdot \epsilon_{\text{coin}})$  at each of the three  $\text{HRS}_e$  field settings. Instead of a collimator, software cuts applied to the recoil protons were used to ensure that the cone of scattered electrons fit entirely into the central flat-acceptance region of the  $\text{HRS}_e$ . This product of efficiencies was  $>99\%$ . Thus, the coincidence efficiency  $\epsilon_{\text{coin}}$  was firmly established at nearly 100%. A nominal systematic uncertainty of  $\pm 1.5\%$  was attributed to  $\epsilon$ .

The quantity  $(L \cdot \epsilon_e)$ , where  $L$  is the luminosity (the product of the effective target thickness and the number of incident electrons) was determined to  $\pm 4\%$  by comparing the

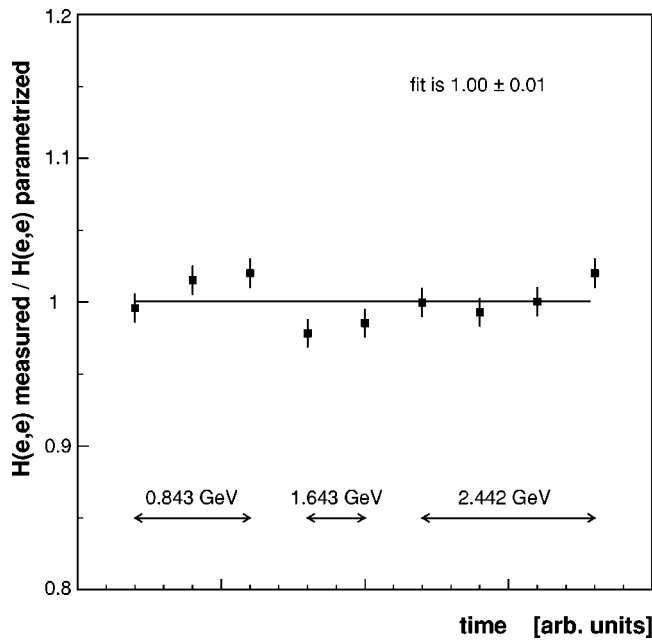


FIG. 4. Measured  $^1\text{H}(e, e)$  cross-section data normalized to the absolute predictions of a parametrization at similar  $Q^2$ . Statistical error bars are shown. The data shown were taken over the course of a three-month run period. The different data points for each  $E_{\text{beam}}$  represent different  $\text{HRS}_h$  angular settings.

measured  $^1\text{H}(e, e)$  cross section for each film at each of the electron kinematics to a parametrization established at a similar  $Q^2$  by Simon *et al.* [64] and Price *et al.* [65] (see Fig. 4). The results reported in this paper have all been normalized in this fashion. As a consistency check, a direct absolute calculation of  $(L \cdot \epsilon_e)$  using information from the BCMs, the calibrated thicknesses of the water films, and the single-arm  $\text{HRS}_e$  efficiency agrees to within uncertainty.

At every kinematics, a Monte Carlo of the phase-space volume subtended by each experimental bin was performed. For each water foil,  $N_0$  software  $(e, e'p)$  events were generated, uniformly distributed over the scattered-electron and knocked-out proton momenta  $(p_e, p_p)$  and in-plane and out-of-plane angles  $(\phi_e, \theta_e, \phi_p, \theta_p)$ . For each of these events, all of the kinematic quantities were calculated. The flat-acceptance cuts determined in the analysis of the relative focal-plane efficiency data were then applied, as were all other cuts that had been performed on the actual data. The pristine detection volume  $\Delta V_b(E_{\text{miss}}, p_{\text{miss}}, \omega, Q^2)$  subtended by a bin  $b(\Delta E_{\text{miss}}, \Delta p_{\text{miss}}, \Delta \omega, \Delta Q^2)$  containing  $N_b$  pseudoevents was thus

$$\Delta V_b(E_{\text{miss}}, p_{\text{miss}}, \omega, Q^2) = \frac{N_b}{N_0} [(\Delta p_e \cdot \Delta \Omega_e) \cdot (\Delta p_p \cdot \Delta \Omega_p)], \quad (2)$$

where the quantity  $(\Delta p_e \cdot \Delta \Omega_e) \cdot (\Delta p_p \cdot \Delta \Omega_p)$  was the total volume sampled over in the Monte Carlo (purposely set larger

than the experimental acceptance in all dimensions<sup>7</sup>). The pseudodata were binned exactly as the real data, and uniformly on both sides of  $\mathbf{q}$ . At each kinematics, the bin with the largest volume  $\Delta V_{\text{max}}$  was located. Only bins subtending volumes larger than 50% of  $\Delta V_{\text{max}}$  were analyzed further.

Corrections based on the TS output-to-input ratio were applied to the data to account for the acquisition deadtime to coincidence events. On average, these corrections were roughly 20%. An acquisition Monte Carlo by Liang [66] was used to cross-check these corrections and establish the absolute uncertainty in them at 2%.

Corrections to the per-film cross-section data for electron radiation before and after scattering were calculated on a bin-by-bin basis in two ways: first using a version of the code RADCOR by Quint [67] modified by Florizone [68], and independently, the prescriptions of Borie and Dreschel [69] modified by Templon *et al.* [70] for use within the simulation package MCEEP written by Ulmer [71]. The two approaches agreed to within the statistical uncertainty of the data and amounted to  $<55\%$  of the measured cross section for the bound states, and  $<15\%$  of the measured cross section for the continuum. Corrections for proton radiation at these energies are much less than 1% and were not performed.

### C. Cross section

The radiatively corrected average cross section in the bin  $b(\Delta E_{\text{miss}}, \Delta p_{\text{miss}}, \Delta \omega, \Delta Q^2)$  was calculated according to

$$\left\langle \frac{d^6\sigma}{d\omega d\Omega_e dE_{\text{miss}} d\Omega_p} \right\rangle_b = \frac{R^{16\text{O}(e, e'p)}}{(L \cdot \epsilon_e)(\epsilon_p \cdot \epsilon_{\text{coin}})} \left( \frac{Y_b}{\Delta V_b} \right), \quad (3)$$

where  $Y_b$  was the total number of real events which were detected in  $b(\Delta E_{\text{miss}}, \Delta p_{\text{miss}}, \Delta \omega, \Delta Q^2)$ ,  $\Delta V_b$  was the phase-space volume, and  $R^{16\text{O}(e, e'p)}$  was a correction applied to account for events which radiated in or out of  $\Delta V_b$ . The average cross section was calculated as a function of  $E_{\text{miss}}$  for a given kinematic setting.<sup>8</sup> Bound-state cross-section data for the  $1p$ -shell were extracted by integrating over the appropriate range in  $E_{\text{miss}}$ , weighting with the appropriate Jacobian.<sup>9</sup>

### D. Asymmetries and response functions

In the One-Photon Exchange Approximation, the unpolarized six-fold differential cross section may be expressed in

<sup>7</sup>When necessary, the differential dependencies of the measured cross-section data were changed to match those employed in the theoretical calculations. The pristine detection volume  $\Delta V_b(E_{\text{miss}}, p_{\text{miss}}, \omega, Q^2)$  was changed to a weighted detection volume by weighting each of the trials with the appropriate Jacobian(s).

<sup>8</sup>The difference between cross-section data averaged over the reduced spectrometer acceptances and calculated for a small region of the central kinematics was no more than 1%. Thus, the finite acceptance of the spectrometers was not an issue.

<sup>9</sup>This Jacobian is given by  $\partial E_{\text{miss}} / \partial p_p = p_p / E_p + \mathbf{p}_p \cdot \mathbf{p}_B / p_p E_B$ , where  $E_B = \sqrt{\mathbf{p}_B^2 + m_B^2}$ .



terms of four independent response functions as (see Refs. [2,9,72])

$$\frac{d^6\sigma}{d\omega d\Omega_e dE_{\text{miss}} d\Omega_p} = K\sigma_{\text{Mott}}[v_L R_L + v_T R_T + v_{LT} R_{LT} \cos(\phi) + v_{TT} R_{TT} \cos(2\phi)], \quad (4)$$

where  $K$  is a phase-space factor,  $\sigma_{\text{Mott}}$  is the Mott cross section, and the  $v_i$  are dimensionless kinematic factors.<sup>10</sup> Ideal response functions are not directly measurable because electron distortion does not permit the azimuthal dependencies to be separated exactly. The effective response functions which are extracted by applying Eq. (4) to the data are denoted  $R_L$  (longitudinal),  $R_T$  (transverse),  $R_{LT}$  (longitudinal-transverse), and  $R_{TT}$  (transverse-transverse). They contain all the information which may be extracted from the hadronic system using  $(e, e'p)$ . Note that the  $v_i$  depend only on  $(\omega, Q^2, \theta_e)$ , while the response functions depend on  $(\omega, Q^2, E_{\text{miss}}, p_{\text{miss}})$ .

The individual contributions of the effective response functions may be separated by performing a series of cross-section measurements varying  $v_i$  and/or  $\phi$ , but keeping  $q$  and  $\omega$  constant.<sup>11</sup> In the case where the proton is knocked-out of the nucleus in a direction parallel to  $\mathbf{q}$  (“parallel” kinematics), the interference terms  $R_{LT}$  and  $R_{TT}$  vanish, and a Rosenbluth separation [73] may be performed to separate  $R_L$  and  $R_T$ . In the case where the proton is knocked-out of the nucleus in the scattering plane with a finite angle  $\theta_{pq}$  with respect to  $\mathbf{q}$  (“quasiperpendicular” kinematics), the asymmetry  $A_{LT}$  and the interference  $R_{LT}$  may be separated by performing symmetric cross-section measurements on either side of  $\mathbf{q}$  ( $\phi=0^\circ$  and  $\phi=180^\circ$ ). The contribution of  $R_{TT}$  cannot be separated from that of  $R_L$  with only in-plane measurements; however, by combining the two techniques, an interesting combination of response functions  $R_T$ ,  $R_{LT}$ , and  $R_{L+TT}$ <sup>12</sup> may be extracted.

For these data, effective response-function separations were performed where the phase-space overlap between kinematics permitted. For these separations, bins were selected only if their phase-space volumes  $\Delta V_b$  were all simultaneously  $\geq 50\%$  of  $\Delta V_{\text{max}}$ .

### E. Systematic uncertainties

The systematic uncertainties in the cross-section measurements were classified into two categories—kinematic-

<sup>10</sup>The phase-space factor  $K$  is given in Eq. (A2), while  $\sigma_{\text{Mott}} = \alpha^2 \cos^2(\theta_e/2) / 4E_{\text{beam}}^2 \sin^4(\theta_e/2)$ . The dimensionless kinematic factors are as follows:  $v_L = Q^4 / \mathbf{q}^4$ ,  $v_T = Q^2 / 2\mathbf{q}^2 + \tan^2(\theta_e/2)$ ,  $v_{LT} = (Q^2 / \mathbf{q}^2) \sqrt{Q^2 / \mathbf{q}^2 + \tan^2(\theta_e/2)}$ , and  $v_{TT} = Q^2 / 2\mathbf{q}^2$ .

<sup>11</sup>The accuracy of the effective response-function separation depends on precisely matching the values of  $q$  and  $\omega$  at each of the different kinematic settings. This precise matching was achieved by measuring  ${}^1\text{H}(e, ep)$  with a pinhole collimator (in practice, the central hole of the sieve-slit collimator) placed in front of the HRS<sub>e</sub>. The measured proton momentum was thus  $q$ . The  ${}^1\text{H}(e, ep)$  proton momentum peak was determined to  $\Delta p/p = 1.5 \times 10^{-4}$ , which allowed for an identical matching of  $q$  for the different kinematic settings.

<sup>12</sup> $R_{L+TT} \equiv R_L + (V_{TT}/V_L)R_{TT}$ .

TABLE III. Kinematic-dependent systematic uncertainties folded into the MCEEP simulation series.

Quantity	Description	$\delta$
$E_{\text{beam}}$	Beam energy	$1.6 \times 10^{-3}$
$\phi_{\text{beam}}$	In-plane beam angle	Ignored <sup>a</sup>
$\theta_{\text{beam}}$	Out-of-plane beam angle	2.0 mrad
$p_e$	Scattered electron momentum	$1.5 \times 10^{-3}$
$\phi_e$	In-plane scattered electron angle	0.3 mrad
$\theta_e$	Out-of-plane scattered electron angle	2.0 mrad
$p_p$	Proton momentum	$1.5 \times 10^{-3}$
$\phi_p$	In-plane proton angle	0.3 mrad
$\theta_p$	Out-of-plane proton angle	2.0 mrad

<sup>a</sup>As previously mentioned, the angle of incidence of the electron beam was determined using a pair of BPMs located upstream of the target (see Fig. 2). The BPM readback was calibrated by comparing the location of survey fiducials along the beamline to the Hall A survey fiducials. Thus, in principle, uncertainty in the knowledge of the incident electron-beam angle should be included in this analysis. However, the simultaneous measurement of the kinematically overdetermined  ${}^1\text{H}(e, ep)$  reaction allowed for a calibration of the absolute kinematics, and thus an elimination of this uncertainty. That is, the direction of the beam defined the axis relative to which all angles were measured via  ${}^1\text{H}(e, ep)$ .

dependent uncertainties and scale uncertainties. For a complete discussion of how these uncertainties were evaluated, the interested reader is directed to a report by Fissum and Ulmer [74]. For the sake of completeness, a subset of the aforementioned information is presented here.

In a series of simulations performed after the experiment, MCEEP was used to investigate the intrinsic behavior of the cross-section data when constituent kinematic parameters were varied over the appropriate experimentally determined ranges presented in Table III. Based on the experimental data, the high- $E_{\text{miss}}$  region was modeled as the superposition of a peak-like  $1s_{1/2}$ -state on a flat continuum. Contributions to the systematic uncertainty from this flat continuum were taken to be small, leaving only those from the  $1s_{1/2}$ -state. The  ${}^{16}\text{O}(e, e'p)$  simulations incorporated as physics input the bound-nucleon RDWIA calculations detailed in Sec. V A, which were based on the experimental  $1p$ -shell data.

For each kinematics, the central water foil was considered, and 1M events were generated. In evaluating the simulation results, the exact cuts applied in the actual data analyses were applied to the pseudo-data, and the cross section was evaluated for the identical  $p_{\text{miss}}$  bins used to present the results. The experimental constraints to the kinematic-dependent observables afforded by the overdetermined  ${}^1\text{H}(e, ep)$  reaction were exploited to calibrate and constrain the experimental setup. The in-plane electron and proton angles  $\phi_e$  and  $\phi_p$  were chosen as independent parameters. When a known shift in  $\phi_e$  was made,  $\phi_p$  was held constant and the complementary variables  $E_{\text{beam}}$ ,  $p_e$ , and  $p_p$  were varied as required by the constraints enforced by the  ${}^1\text{H}(e, ep)$  reaction. Similarly, when a known shift in  $\phi_p$  was made,  $\phi_e$  was held constant and the complementary variables  $E_{\text{beam}}$ ,  $p_e$ , and  $p_p$  were varied as appropriate. The overall con-



TABLE IV. A summary of the scale systematic uncertainties contributing to the cross-section data. The first seven entries do not contribute to the systematic uncertainties in the reported cross-section data as they contribute equally to the  $^1\text{H}(e, e)$  cross-section data to which the  $^{16}\text{O}(e, e'p)$  data are normalized.

Quantity	Description	$\delta$ (%)
$\eta_{\text{DAQ}}$	Data acquisition deadtime correction	2.0
$\eta_{\text{elec}}$	Electronics deadtime correction	<1.0
$\rho t'$	Effective target thickness	2.5
$N_e$	Number of incident electrons	2.0
$\epsilon_e$	Electron detection efficiency	1.0
$\Delta\Omega_e^{\text{a}}$	HRS <sub>e</sub> solid angle	2.0
$\epsilon_e \cdot \epsilon_p \cdot \epsilon_{\text{coin}}$	Product of electron, proton, and coincidence efficiencies	1.5
$L \cdot \epsilon_e$	Obtained from a form-factor parametrization of $^1\text{H}(e, e)$	4.0
$R_{^{16}\text{O}(e, e'p)}^{\text{b}}$	Radiative correction to the $^{16}\text{O}(e, e'p)$ data	2.0
$R_{^1\text{H}(e, e)}^{\text{b}}$	Radiative correction to the $^1\text{H}(e, e)$ data	2.0
$\epsilon_p \cdot \epsilon_{\text{coin}}$	Product of proton and coincidence efficiencies	<1.0
$\Delta\Omega_p^{\text{a}}$	HRS <sub>h</sub> solid angle	2.0
Punchthrough <sup>c</sup>	Protons which punched through the HRS <sub>h</sub> collimator	2.0

<sup>a</sup>The systematic uncertainties in the solid angles  $\Delta\Omega_e$  and  $\Delta\Omega_p$  were quantified by studying sieve-slit collimator optics data at each of the spectrometer central momenta employed. The angular locations of each of the reconstructed peaks corresponding to the  $7 \times 7$  lattice of holes in the sieve-slit plate were compared to the locations predicted by spectrometer surveys, and the overall uncertainty was taken to be the quadratic sum of the individual uncertainties.

<sup>b</sup>At first glance, it may be surprising to note that the uncertainty due to the radiative correction to the data is included as a scale uncertainty. In general, the radiative correction is strongly dependent on kinematics. However, the  $1p$ -shell data analysis, and for that matter any bound-state data analysis, involves  $E_{\text{miss}}$  cuts. These cuts to a large extent remove the strong kinematic dependence of the radiative correction, since only relatively small photon energies are involved. In order to compensate for any remaining weak kinematic dependence, the uncertainty due to the radiative correction was slightly overestimated.

<sup>c</sup>High  $E_{\text{miss}}$  data only.

strained uncertainty was taken to be the quadratic sum of the two contributions.

The global convergence of the uncertainty estimate was examined for certain extreme kinematics, where 10M-event simulations (which demonstrated the same behavior) were performed. The behavior of the uncertainty as a function of  $p_{\text{miss}}$  was also investigated by examining the uncertainty in the momentum bins adjacent to the reported momentum bin in exactly the same fashion. The kinematically induced systematic uncertainty in the  $^{16}\text{O}(e, e'p)$  cross-section data was determined to be dependent upon  $p_{\text{miss}}$ , with an average value of 1.4%. The corresponding uncertainties in the  $^1\text{H}(e, e)$  cross-section data were determined to be negligible.

The scale systematic uncertainties which affect each of the cross-section measurements are presented in Table IV. As previously mentioned, the  $^{16}\text{O}(e, e'p)$  cross-section results reported in this paper have been normalized by comparing simultaneously measured  $^1\text{H}(e, e)$  cross-section data to a parametrization established at a similar  $Q^2$ . Thus, the first seven listed uncertainties simply divide out of the quotient, such that only the subsequent uncertainties affect the results. The average systematic uncertainty associated with a  $1p$ -shell cross section was 5.6%, while that for the continuum was 5.9%. The small difference was due to contamination of the high- $E_{\text{miss}}$  data by collimator punch-through events.

The quality of these data in terms of their associated systematic uncertainties was clearly demonstrated by the results obtained for the effective response-function separations. In Fig. 5, cross-section data for the  $1p$ -shell measured in parallel kinematics at three different beam energies are shown as a function of the separation lever arm  $v_T/v_L$ . The values of the effective response functions  $R_L$  (offset) and  $R_T$  (slope) were extracted from the fitted line. The extremely linear trend in the data indicated that the magnitude of the systematic uncertainties was small, and that statistical uncertainties dominated. This is not simply a test of the One-Photon Exchange Approximation (OPEA) employed in the data analysis as it has been demonstrated by Traini *et al.* [75] and Udías [76] that the linear behavior of the Rosenbluth plot

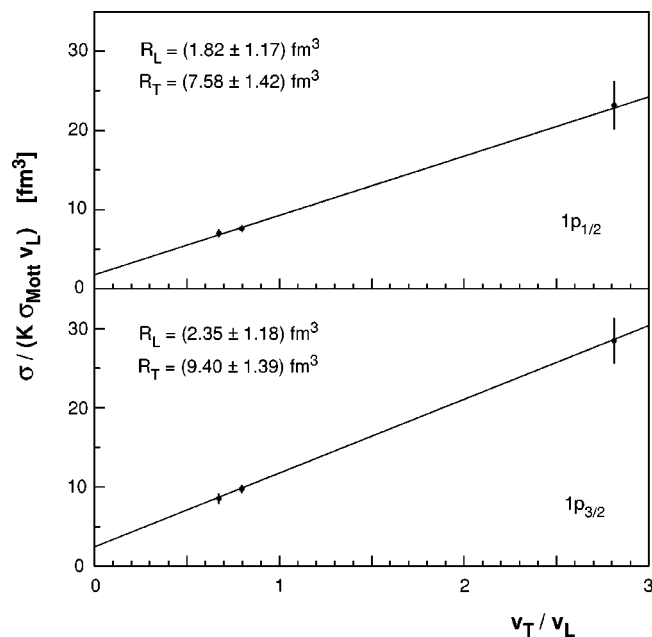


FIG. 5. Cross-section data for the removal of protons from the  $1p$ -shell of  $^{16}\text{O}$  measured in parallel kinematics at three different beam energies as a function of the separation lever arm  $v_T/v_L$ . The data points correspond to beam energies of 2.442, 1.643, and 0.843 GeV from left to right. The effective response functions  $R_L$  (offset) and  $R_T$  (slope) have been extracted from the fitted line. The uncertainties shown are statistical only. The extremely linear behavior of the data (which persists even after corrections for Coulomb distortion are applied) indicates that the statistical uncertainties were dominant (see Sec. III E for a complete discussion).

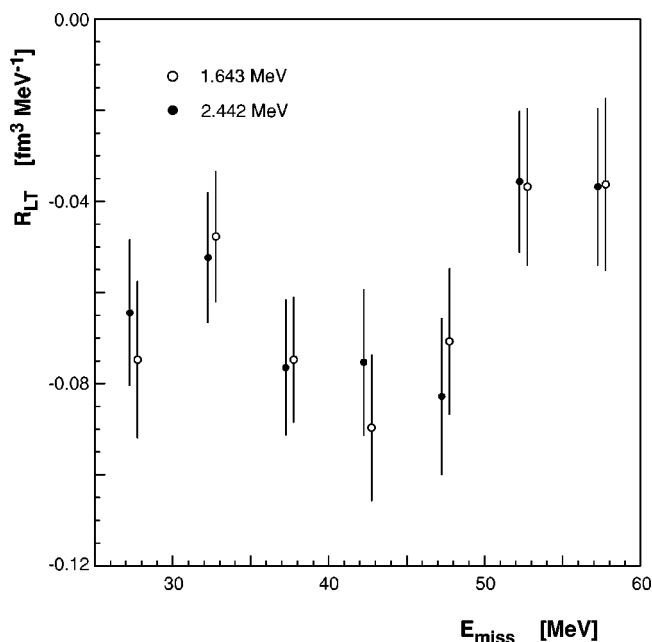


FIG. 6.  $R_{LT}$  for  $\theta_{pq} = \pm 8^\circ$  ( $p_{\text{miss}} = 145 \text{ MeV}/c$ ) as a function of  $E_{\text{miss}}$  for  $E_{\text{beam}} = 1.643 \text{ GeV}$  and  $2.442 \text{ GeV}$ . Statistical uncertainties only are shown. The statistical agreement over a broad range of  $E_{\text{miss}}$  emphasizes the systematic precision of the measurement (see Sec. III E for a complete discussion). Note that the averages of these  $R_{LT}$  values are presented as the  $p_{\text{miss}} = 145 \text{ MeV}/c$  data in Fig. 22.

persists even after Coulomb distortion is included.

Given the applicability of the OPEA at these energies, the quality of the data was also demonstrated by the results extracted from identical measurements which were performed in different electron kinematics. The asymmetries  $A_{LT}$  and effective response functions  $R_{LT}$  for QE proton knockout were extracted for both  $E_{\text{beam}} = 1.643 \text{ GeV}$  and  $2.442 \text{ GeV}$  for  $\theta_{pq} = \pm 8^\circ$  ( $p_{\text{miss}} = 148 \text{ MeV}/c$ ). They agree within the statistical uncertainty. Figure 6 shows the  $R_{LT}$  results for  $1p$ -shell knockout for  $\langle Q^2 \rangle \approx 0.8 \text{ (GeV}/c)^2$ ,  $\langle \omega \rangle = 436 \text{ MeV}$ ,  $\langle T_p \rangle = 427 \text{ MeV}$ , and  $25 < E_{\text{miss}} < 60 \text{ MeV}$ .

#### IV. THEORETICAL PRIMER

In Sec. V, the data will be compared with calculations based upon three different approaches where the overlap between initial and final nuclear states differing by a single proton is represented by a bound state of the Dirac equation. In this section, comparisons are first made between each of these approaches. The most important differences are found in the treatment of the FSI.

The Relativistic Distorted-Wave Impulse Approximation (RDWIA) uses a partial-wave expansion of the Dirac equation with complex scalar and vector potentials. Comparisons presented in Sec. IV A show that two different implementations based upon either first- or second-order representations of the Dirac equation yield equivalent results. The Relativistic Optical-Model Eikonal Approximation (ROMEIA) employs an Eikonal Approximation (EA) that should be equiva-

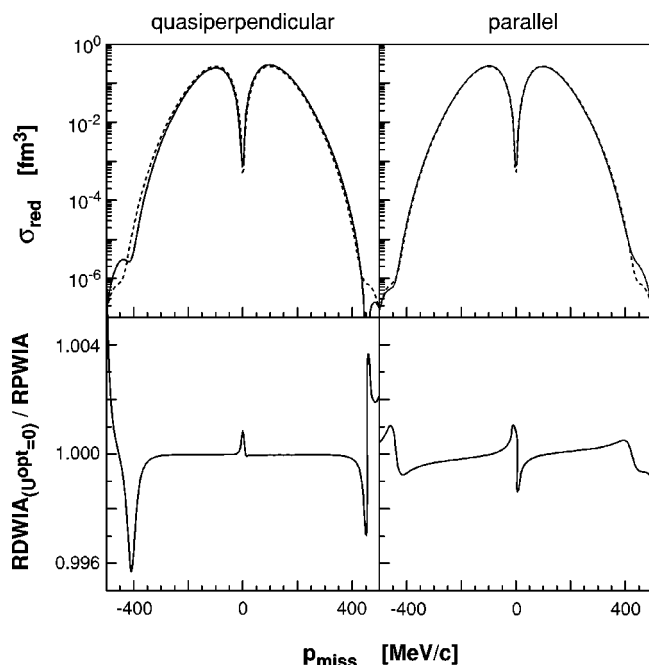


FIG. 7. Comparisons between RPWIA and  $\text{RDWIA}_{(U^{\text{opt}}=0)}$  calculations for the removal of protons from the  $1p_{1/2}$ -state of  $^{16}\text{O}$  as a function of  $p_{\text{miss}}$  for  $E_{\text{beam}} = 2.442 \text{ GeV}$ . In the upper panels, the solid curves represent the reduced cross section for both the  $\text{RDWIA}_{(U^{\text{opt}}=0)}$  and the RPWIA calculations (see the text for details). The dashed curves correspond to the momentum distributions. In the lower panels,  $\text{RDWIA}_{(U^{\text{opt}}=0)}/\text{RPWIA}$  reduced cross-section ratios are shown. Agreement to much better than 1% is obtained for both kinematics over the entire  $p_{\text{miss}}$  range.

lent to RDWIA for large  $Q^2$ , but more efficient because a partial-wave expansion is avoided. The Relativistic Multiple-Scattering Glauber Approximation (RMSGGA) also uses the EA but instead evaluates multiple scattering by the nucleon-nucleon ( $NN$ ) interaction directly rather than through a mean field. Comparisons between the (RDWIA and ROMEIA) and RMSGGA approaches are presented in Sec. IV B.

#### A. RDWIA

As previously mentioned, the Relativistic Distorted-Wave Impulse Approximation (RDWIA) was pioneered by Picklesimer, Van Orden, and Wallace [7–9] and subsequently developed in more detail by several groups (see Refs. [16,21,77–81]). The RDWIA formalism is presented in detail in Appendix A 1.

Figure 7 illustrates a comparison between the Relativistic Plane-Wave Impulse Approximation (RPWIA) and  $\text{RDWIA}_{(U^{\text{opt}}=0)}$  calculations made by Kelly using LEA for the removal of protons from the  $1p_{1/2}$ -state of  $^{16}\text{O}$  as a function of  $p_{\text{miss}}$  for both quasiperpendicular and parallel kinematics for  $E_{\text{beam}} = 2.442 \text{ GeV}$ .

The  $\text{RDWIA}_{(U^{\text{opt}}=0)}$  calculations employed a partial-wave expansion of the second-order Dirac equation with optical potentials nullified and the target mass artificially set to  $16001u$  to minimize recoil corrections and frame ambiguities. The RPWIA calculations (see Ref. [5]) are based upon

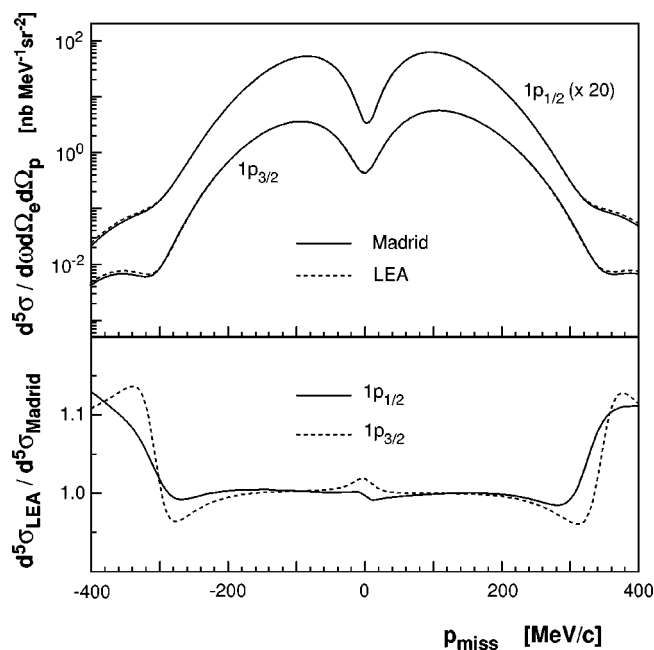


FIG. 8. Comparison baseline RDWIA calculations by the Madrid Group and Kelly (LEA) for the removal of protons from the  $1p$ -shell of  $^{16}\text{O}$  as a function of  $p_{\text{miss}}$  for  $E_{\text{beam}}=2.442$  GeV. For the purposes of this comparison, the input into both calculations was identical (see Table V). Overall agreement is very good, and agreement is excellent for  $-250 < p_{\text{miss}} < 250$  MeV/ $c$ .

the Fourier transforms of the upper and lower components of the overlap function; that is, no partial-wave expansion is involved. In the upper panels, the solid curves represent the reduced cross section for both the  $\text{RDWIA}_{(U^{\text{opt}}=0)}$  and  $\text{RPWIA}$  calculations as the differences are indistinguishable on this scale. The dashed curves show the momentum distributions. In the lower panels, the ratios between  $\text{RDWIA}_{(U^{\text{opt}}=0)}$  and  $\text{RPWIA}$  reduced cross sections are shown. With suitable choices for step size and maximum  $\ell$  (here 0.05 fm and 80), agreement to much better than 1% over the entire range of missing momentum is obtained, verifying the accuracy of LEA for plane waves. Similar results are obtained with the Madrid code of Udías *et al.* (see below).

The similarity between the reduced cross sections and the momentum distributions demonstrates that the violation of factorization produced by the distortion of the bound-state spinor is mild, but tends to increase with  $p_{\text{miss}}$ . Nevertheless, observables such as  $A_{LT}$  that are sensitive to the interference between the lower and upper components are more strongly affected by the violation of factorization.

Figures 8 and 9 compare calculations for the removal of protons from the  $1p$ -shell of  $^{16}\text{O}$  as a function of  $p_{\text{miss}}$  for  $E_{\text{beam}}=2.442$  GeV. The calculations made by Kelly [82] using LEA employ a second-order representation of the Dirac equation while those of the Madrid group use the standard first-order representation. Both calculations employ the set of baseline options summarized in Table V, which were chosen to provide the most rigorous numerical test of the codes without necessarily being optimal physics choices.

Figure 8 demonstrates that baseline cross-section calculations agree to better than 2% for  $p_{\text{miss}} < 250$  MeV/ $c$ , but that

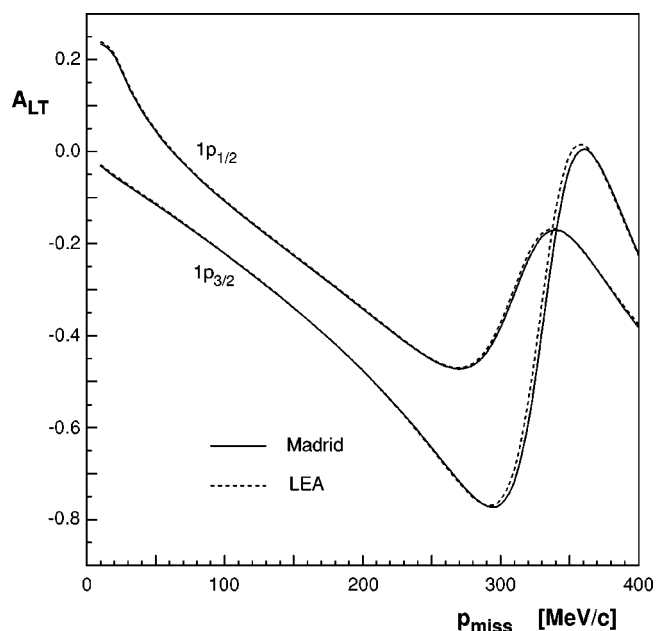


FIG. 9. Comparison baseline RDWIA calculations for the  $A_{LT}$  asymmetry by the Madrid Group and Kelly (LEA) for the removal of protons from the  $1p$ -shell of  $^{16}\text{O}$  as a function of  $p_{\text{miss}}$  for  $E_{\text{beam}}=2.442$  GeV. For the purposes of this comparison, the input into both calculations was identical (see Table V). Overall agreement is excellent over the entire  $p_{\text{miss}}$  range.

the differences increase to about 10% by about 400 MeV/ $c$ . Nevertheless, Fig. 9 shows that excellent agreement is obtained for  $A_{LT}$  over this entire range of  $p_{\text{miss}}$ , with only a very small observable shift. The agreement of the strong oscillations in  $A_{LT}$  for  $p_{\text{miss}} \approx 300$  MeV/ $c$  predicted by both methods demonstrates that they are equivalent with respect to spinor distortion. The small differences in the cross section for large  $p_{\text{miss}}$  appear to be independent of the input choices and probably arise from numerical errors in the integration of differential equations (perhaps due to initial conditions), but the origin has not yet been identified. Regardless, it is remarkable to achieve this level of agreement between two independent codes under conditions in which the cross section spans three orders of magnitude.

TABLE V. A summary of the basic RDWIA options which served as input to the “baseline” comparison calculations of the Madrid Group and Kelly (LEA). Results are shown in Figs. 8 and 9.

Input parameter	Option
Bound-nucleon wave function	NLSH—Sharma <i>et al.</i> [83]
Optical Model	EDAI-O—Cooper <i>et al.</i> [84]
Nucleon spinor distortion	Relativistic
Electron distortion	None
Current operator	CC2
Nucleon form factors	Dipole
Gauge	Coulomb

TABLE VI. A summary of the basic options which served as input to the comparison between the RDWIA calculations and the “bare” RMSGA (no MEC nor IC) calculations of the Ghent Group. Results are shown in Fig. 10.

Input parameter	Option
Bound-nucleon wave function	Furnstahl <i>et al.</i> [90]
Optical Model	EDAI-O
Nucleon spinor distortion	Relativistic
Electron distortion	None
Current operator	CC2
Nucleon form factors	Dipole
Gauge	Coulomb

### B. ROMEA/RMSGGA

The alternate relativistic model developed by the Ghent Group [85–88] for  $A(e, e'N)B$  processes is presented in Appendix A 2. With respect to the construction of the bound-nucleon wave functions and the nuclear-current operator, an approach similar to standard RDWIA is followed. The (RDWIA and ROMEA) and RMSGA frameworks are substantially different in the way they address FSI. While the RDWIA and ROMEA models are both essentially one-body approaches in which all FSI effects are implemented through effective potentials, the RMSGA framework is a full-fledged, multi-nucleon scattering model based on the EA and the concept of frozen spectators. As such, when formulated in an unfactorized and relativistic framework, Glauber calculations are numerically involved and the process of computing the scattering state and the transition matrix elements involves numerical methods which are different from those adopted in RDWIA frameworks. For example, for  $A(e, e'N)B$  calculations in the ROMEA and the RMSGA, partial-wave expansions are simply not a viable option.

The testing of the mutual consistency of the RDWIA and “bare” RMSGA [no meson-exchange currents (MEC) nor isobar currents (IC)] calculations began by considering the special case of vanishing FSI. In this limit, where all the Glauber phases are nullified in RMSGA and (RDWIA→RPWIA), the two calculations were determined to reproduce one another to 4% over the entire  $p_{\text{miss}}$  range, thereby establishing the validity of the numerics. The Glauber phases were then enabled. The basic options which then served as input to the comparison between the RDWIA calculations and the RMSGA calculations of the Ghent Group [89] are presented in Table VI.

Figure 10 shows the ratio of the bare RMSGA calculations of the Ghent Group together with RDWIA calculations for the removal of protons from the  $1p$ -shell of  $^{16}\text{O}$  as a function of  $p_{\text{miss}}$  for  $E_{\text{beam}} = 2.442$  GeV. Apart from the treatment of FSI, all other ingredients to the calculations are identical (see Table VI). For  $p_{\text{miss}}$  below the Fermi momentum, the variation between the predictions of the two approaches is at most 25%, with the RDWIA approach predicting a smaller cross section (stronger absorptive effects) than the RMSGA model. Not surprisingly, at larger  $p_{\text{miss}}$  (correspondingly larger polar angles), the differences between the two approaches grow.

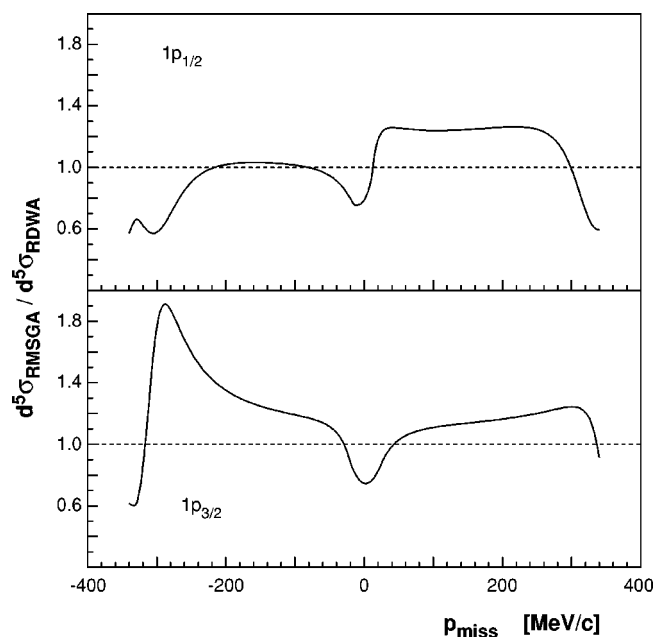


FIG. 10. RDWIA calculations compared to “bare” (no MEC nor IC) RMSGA calculations by the Ghent Group for the removal of protons from the  $1p$ -shell of  $^{16}\text{O}$  as a function of  $p_{\text{miss}}$  for  $E_{\text{beam}} = 2.442$  GeV. Both calculations employ the input presented in Table VI. Apart from the treatment of FSI, all ingredients are identical.

## V. RESULTS FOR $Q^2 \approx 0.8$ (GeV/c)<sup>2</sup>

The data were interpreted in subsets corresponding to the  $1p$ -shell and to the  $1s_{1/2}$ -state and continuum. The interested reader is directed to the works of Gao *et al.* [91] and Liyanage *et al.* [92], where these results have been briefly highlighted. Note that when data are presented in the following discussion, statistical uncertainties only are shown. For a complete archive of the data, including systematic uncertainties, please see our deposit at the EPAPS website [132].

### A. $1p$ -shell knockout

#### 1. Sensitivity to RDWIA variations

The consistency of the normalization factors  $S_\alpha$  suggested by the  $1p$ -shell data for  $p_{\text{miss}} < 350$  MeV/c obtained in this measurement at 2.442 GeV was examined within the RDWIA framework in a detailed study by the Madrid Group [93]. The study involved systematically varying a wide range of inputs to the RDWIA calculations, and then performing least-squares fits of the predictions to the cross-section data. The results of the study are presented in Table VII.

Three basic approaches were considered: the fully relativistic approach, the projected approach of Udías *et al.* [20,21], and the EMA-noSV (EMA denotes the Effective Momentum Approximation) approach of Kelly [4,94]. All three approaches included the effects of electron distortion. While the fully relativistic approach involved solving the Dirac equation directly in configuration space, the projected approach included only the positive-energy components, and as a result, most (but not all) of the spinor distortion was removed from the wave functions. Within the EMA-noSV ap-



TABLE VII. Normalization factors derived from the 2.442 GeV  $1p$ -shell cross-section data using the CC1 and CC2 current operators. The first term in each column is for the  $1p_{1/2}$ -state, while the second term is for the  $1p_{3/2}$ -state.

Prescription		Bound-nucleon wave function	Gauge			Optical potential				Nucleon FF model		Doublet (%)			$S_\alpha$		$\chi^2$										
Fully rel	proj	EMA-noSV	NLS			EDA							GK+	d	QMC	100	50	0	CC1	CC2	CC1	CC2					
			H	H-P	HS	C	W	L	I-O	D1	D2	MRW											RLF	GK			
*			*			*				*				*			*			0.68	0.62	0.74	0.67	5.5	5.3	2.0	31.0
	*		*			*				*				*			*			0.78	0.73	0.76	0.71	17.0	79.0	8.0	70.0
		*	*			*				*				*			*			0.72	0.66	0.75	0.69	2.3	65.0	2.2	65.0
*				*		*				*				*			*			0.60	0.52	0.63	0.54	10.0	97.0	15.0	115.0
*					*	*				*				*			*			0.62	0.61	0.65	0.65	10.0	6.7	18.0	41.0
*			*			*				*				*			*			0.63	0.59	0.76	0.70	25.0	9.2	2.6	22.0
*			*			*				*				*			*			0.69	0.63	0.73	0.67	3.7	6.4	2.5	34.0
*			*			*				*			*				*			0.64	0.60	0.72	0.67	29.0	12.0	4.8	8.2
*			*			*				*			*				*			0.64	0.59	0.71	0.65	15.0	6.4	0.7	15.0
*			*			*				*			*				*			0.62	0.60	0.71	0.67	35.0	11.0	7.6	7.3
*			*			*				*			*				*			0.61	0.58	0.70	0.65	41.0	12.0	6.1	7.9
*			*			*				*			*			*				0.69	0.63	0.75	0.68	4.8	5.9	2.1	31.0
*			*			*				*			*				*			0.65	0.61	0.72	0.66	11.0	3.3	0.5	16.0
*			*			*				*			*				*			0.64		0.70			6.1		33.0
*			*			*				*			*				*			0.66		0.72			7.4		35.0

034606-13

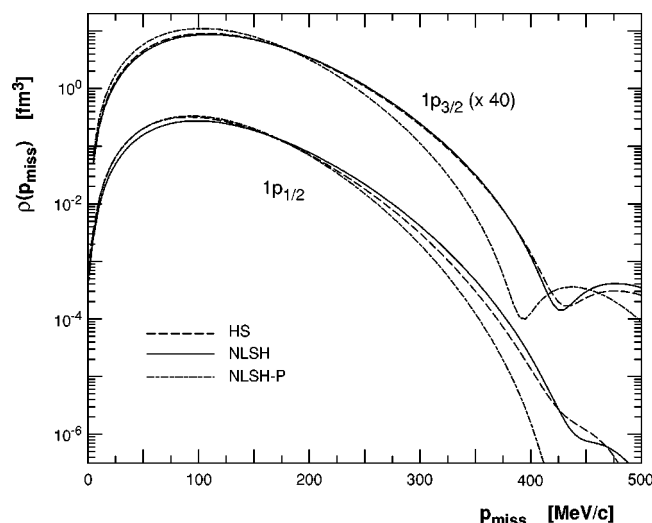


FIG. 11. Momentum distributions for the HS, NLSH, and NLSH-P models. There is only a slight difference between HS and NLSH—for the  $1p_{3/2}$ -state, HS is broader spatially and thus drops off faster with increasing  $p_{\text{miss}}$ . On the other hand, NLSH-P differs appreciably from both HS and NLSH, and is clearly distinguishable for  $p_{\text{miss}} > 250$  MeV/ $c$  for both the  $1p_{1/2}$ - and  $1p_{3/2}$ -states. Note that both the NLSH and NLSH-P wave functions predict binding energies, single-particle energies, and a charge radius for  $^{16}\text{O}$  which are all in good agreement with the data.

proach, a relativized Schrödinger equation was solved using the EMA, and all of the spinor distortion was removed. This made the calculation similar to a factorized calculation, although spin-orbit effects in the initial and final states (which cause small deviations from the factorized results) are included in EMA-noSV.

The current operator was changed between CC1 and CC2. Three bound-nucleon wave functions (see Fig. 11) derived from relativistic Lagrangians were considered: HS by Horowitz and Serot [95,96], NLSH by Sharma *et al.* [83], and NLSH-P by Udías *et al.* [97] (which resulted from a Lagrangian fine-tuned to reproduce the Leuschner *et al.* data). Note that both the NLSH and NLSH-P wave functions predict binding energies, single-particle energies, and a charge radius for  $^{16}\text{O}$  which are all in good agreement with the data.

The gauge prescription was changed between Coulomb, Weyl, and Landau. The nucleon distortion was evaluated using three purely phenomenological  $SV$  optical potentials (EDAI-O, EDAD1, and EDAD2) by Cooper *et al.* [84], as well as MRW by McNeil *et al.* [98] and RLF by Horowitz [99] and Murdock [100]. The nucleon form-factor model was changed between GK by Gari and Krümpelmann [101] and the dipole model. Further, the QMC model of Lu *et al.* [102,103] predicts a density dependence for form factors that was calculated and applied to the GK form factors using the Local Density Approximation (LDA—see Ref. [80]).

Note that the calculations for the  $1p_{3/2}$ -state include the incoherent contributions of the unresolved  $2s_{1/2}1d_{5/2}$ -doublet. The bound-nucleon wave functions for these positive-parity states were taken from the parametriza-

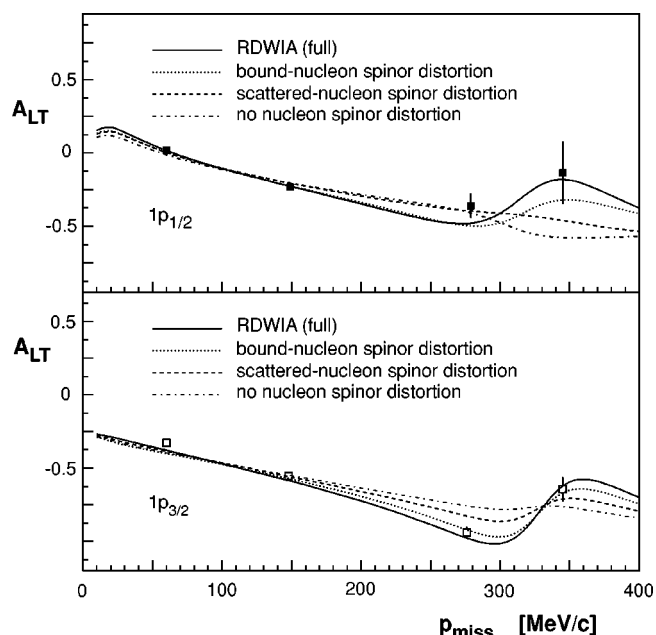


FIG. 12. Left-right asymmetry  $A_{LT}$  together with RDWIA calculations for the removal of protons from the  $1p$ -shell of  $^{16}\text{O}$  as a function of  $p_{\text{miss}}$  for  $E_{\text{beam}} = 2.442$  GeV. Uncertainties are statistical. Note that the solid curves shown here are identical to those shown in Figs. 13 and 15.

tion of Leuschner *et al.* and normalization factors were fit to said data using RDWIA calculations. Factors for both states of 0.12(3) relative to full occupancy were determined. The sensitivity of the present data to this incoherent admixture was evaluated by scaling the fitted doublet contribution using factors of 0.0, 0.5, and 1.0.

Qualitatively, the fully relativistic approach clearly did the best job of reproducing the data. Fully relativistic results were shown to be much less gauge-dependent than the non-relativistic results. The CC2 current operator was in general less sensitive to choice of gauge, and the data discouraged the choice of the Weyl gauge. The different optical models had little effect on the shape of the calculations, but instead changed the overall magnitude. Both the GK and dipole nucleon form-factor models produced nearly identical results. The change in the calculated GK+QMC cross section was modest, being most pronounced in  $A_{LT}$  for  $p_{\text{miss}} > 300$  MeV/ $c$ . The results were best for a 100% contribution of the strength of the  $2s_{1/2}1d_{5/2}$ -doublet to the  $1p_{3/2}$ -state, although the data were not terribly sensitive to this degree of freedom.

Figure 12 shows the left-right asymmetry  $A_{LT}$  together with RDWIA calculations for the removal of protons from the  $1p$ -shell of  $^{16}\text{O}$  as a function of  $p_{\text{miss}}$  for  $E_{\text{beam}} = 2.442$  GeV. The origin of the large change in the slope of  $A_{LT}$  at  $p_{\text{miss}} \approx 300$  MeV/ $c$  is addressed by the various calculations. This “ripple” effect is due to the distortion of the bound-nucleon and ejectile spinors, as evidenced by the other three curves shown, in which the full RDWIA calculations have been decomposed. It is important to note that these three curves all retain the same basic ingredients, par-

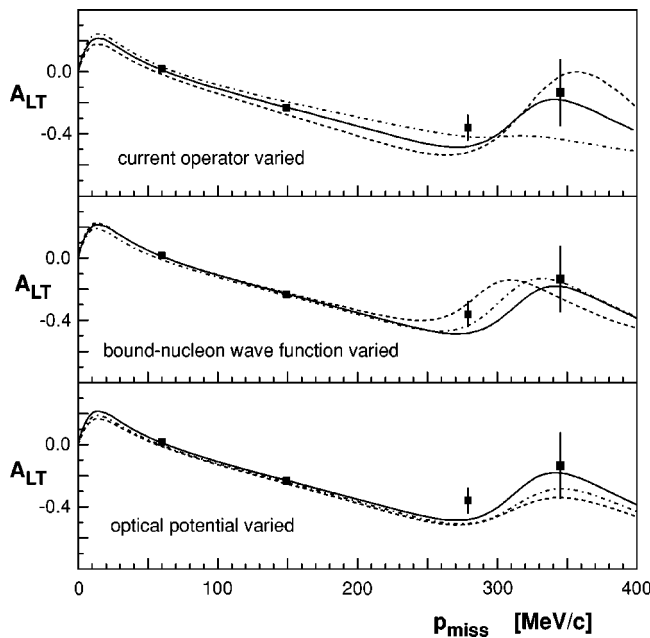


FIG. 13. Left-right asymmetry  $A_{LT}$  together with RDWIA calculations for the removal of protons from the  $1p_{1/2}$ -state of  $^{16}\text{O}$  as a function of  $p_{\text{miss}}$  for  $E_{\text{beam}}=2.442$  GeV. Uncertainties are statistical. The solid curves in all three panels are the same and are identical to those shown for the removal of protons from the  $1p_{1/2}$ -state of  $^{16}\text{O}$  in Figs. 12 and 15.

ticularly the fully relativistic current operator and the upper components of the Dirac spinors. Of the three curves, the dotted line resulted from a calculation where only the bound-nucleon spinor distortion was included, the dashed line resulted from a calculation where only the scattered-state spinor distortion was included, and the dashed-dotted line resulted from a calculation where undistorted spinors (essentially identical to a factorized calculation) were considered. Clearly, the inclusion of the bound-nucleon spinor distortion is more important than the inclusion of the scattered-state spinor distortion, but both are necessary to describe the data.

The effects of variations in the ingredients to the calculations of the left-right asymmetry  $A_{LT}$  for the  $1p_{1/2}$ -state only are shown in Fig. 13. Note that the data are identical to those presented in Fig. 12, as are the solid curves. In the top panel, the EDAl-O optical potential and NLSH bound-nucleon wave function were used for all the calculations, but the choice of current operator was varied between CC1 (dashed), CC2 (solid), and CC3 (dashed-dotted), resulting in a change in both the height and the  $p_{\text{miss}}$ -location of the ripple in  $A_{LT}$ . In the middle panel, the current operator CC2 and EDAl-O optical potential were used for all the calculations, but the choice of bound-nucleon wave function was varied between NLSH-P (dashed), NLSH (solid), and HS (dashed-dotted), resulting in a change in the  $p_{\text{miss}}$ -location of the ripple, but a relatively constant height. In the bottom panel, the current operator CC2 and NLSH bound-nucleon wave function were used for all the calculations, but the choice of optical potential was varied between EDAD1 (dashed), EDAl-O (solid), and EDAD2 (dashed-dotted), resulting in a change in the height of the ripple, but a relatively constant  $p_{\text{miss}}$ -location.

TABLE VIII. A summary of the basic options which served as input to the single-nucleon current RDWIA, ROMEA, and RMSGA comparison calculations. Results are shown in Figs. 14–16.

Input parameter	RDWIA	ROMEA and RMSGA
Bound-nucleon wave function	NLSH	HS
Optical Model	EDAl-O	EDAl-O
Nucleon spinor distortion	Relativistic	Relativistic
Electron distortion	Yes	Yes
Current operator	CC2	CC2
Nucleon form factors	GK	Dipole
Gauge	Coulomb	Coulomb

More high-precision data, particularly for  $150 < p_{\text{miss}} < 400$  MeV/c, are clearly needed to accurately and simultaneously determine the current operator, the bound-state wave function, the optical potential, and of course the normalization factors. This experiment has recently been performed in Hall A at Jefferson Lab by Saha *et al.* [104], and the results are currently under analysis.

## 2. Comparison to RDWIA, ROMEA, and RMSGA calculations considering single-nucleon currents

In this section, the data are compared to RDWIA and bare ROMEA and RMSGA calculations (which take into consideration single-nucleon currents only—no MEC or IC). The basic options employed in the calculations are summarized

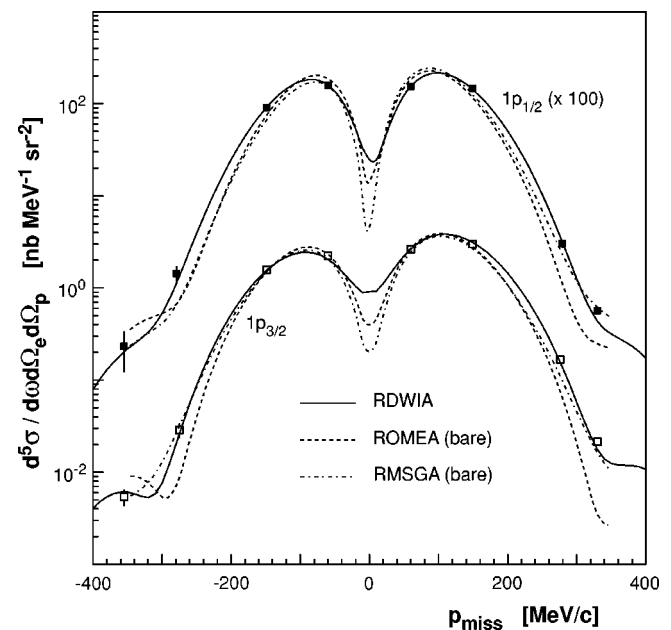


FIG. 14. Measured cross-section data for the removal of protons from the  $1p$ -shell of  $^{16}\text{O}$  as a function of  $p_{\text{miss}}$  as compared to relativistic calculations at  $E_{\text{beam}}=2.442$  GeV. Uncertainties are statistical and, on average, there is an additional  $\pm 5.6\%$  systematic uncertainty associated with the data. The solid line is the RDWIA calculation, while the dashed and dashed-dotted lines are, respectively, the bare ROMEA and RMSGA calculations.

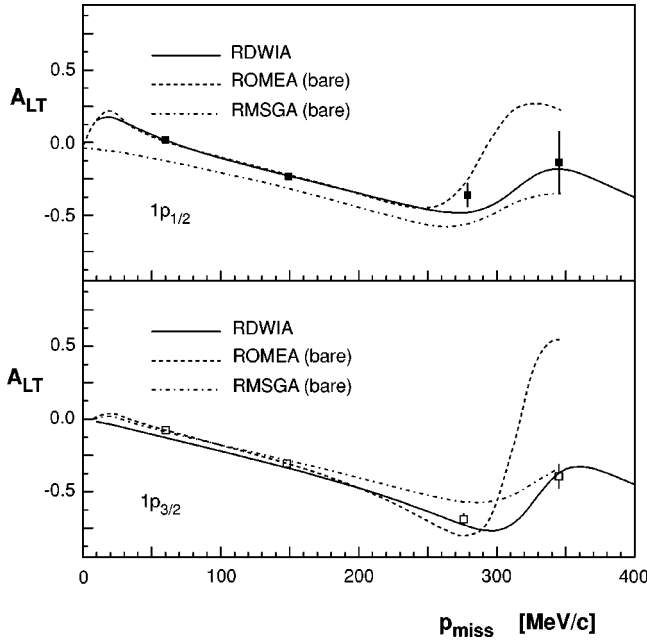


FIG. 15. Left-right asymmetry  $A_{LT}$  together with relativistic calculations of the  $A_{LT}$  asymmetry for the removal of protons from the  $1p$ -shell of  $^{16}\text{O}$  as a function of  $p_{\text{miss}}$  for  $E_{\text{beam}}=2.442$  GeV. Uncertainties are statistical. The solid line is the RDWIA calculation, while the dashed and dashed-dotted lines are, respectively, the bare ROMEA and RMSGA calculations. Note that the solid curves shown here are identical to those shown in Figs. 12 and 13.

in Table VIII. Note that both the EA-based calculations stop at  $p_{\text{miss}}=350$  MeV/ $c$  as the approximation becomes invalid.

Figure 14 shows measured cross-section data for the removal of protons from the  $1p$ -shell of  $^{16}\text{O}$  as a function of  $p_{\text{miss}}$  as compared to relativistic calculations at  $E_{\text{beam}}=2.442$  GeV. The solid line is the RDWIA calculation, while the dashed and dashed-dotted lines are, respectively, the bare ROMEA and RMSGA calculations. The normalization factors for the RDWIA calculations are 0.73 and 0.72 for the  $1p_{1/2}$ -state and  $1p_{3/2}$ -state, respectively. For the ROMEA and RMSGA calculations, they are 0.6 and 0.7 for the  $1p_{1/2}$ -state and  $1p_{3/2}$ -state, respectively. The RDWIA calculations do a far better job of representing the data over the entire  $p_{\text{miss}}$  range.

Figure 15 shows the left-right asymmetry  $A_{LT}$  together with relativistic calculations for the removal of protons from the  $1p$ -shell of  $^{16}\text{O}$  as a function of  $p_{\text{miss}}$  for  $E_{\text{beam}}=2.442$  GeV. The solid line is the RDWIA calculation, while the dashed and dashed-dotted lines are, respectively, the bare ROMEA and RMSGA calculations. Note again the large change in the slope of  $A_{LT}$  at  $p_{\text{miss}}\approx 300$  MeV/ $c$ . While all three calculations undergo a similar change in slope, the RDWIA calculation does the best job of reproducing the data. The ROMEA calculation reproduces the data well for  $p_{\text{miss}} < 300$  MeV/ $c$ , but substantially overestimates  $A_{LT}$  for  $p_{\text{miss}} > 300$  MeV/ $c$ . The RMSGA calculation does well with the overall trend in the data, but struggles with reproducing the data for the  $1p_{1/2}$ -state.

Figure 16 shows the  $R_{L+TT}$ ,  $R_{LT}$ , and  $R_T$  effective response functions together with relativistic calculations for the re-

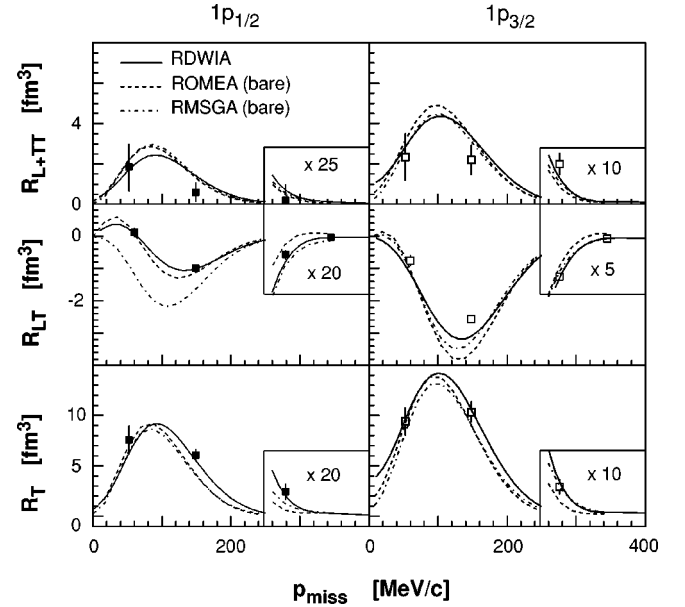


FIG. 16. Data from this work together with relativistic calculations for the  $R_{L+TT}$ ,  $R_{LT}$ , and  $R_T$  effective response functions for the removal of protons from the  $1p$ -shell of  $^{16}\text{O}$  as a function of  $p_{\text{miss}}$ . Uncertainties are statistical. The solid line is the RDWIA calculation, while the dashed and dashed-dotted lines are, respectively, the bare ROMEA and RMSGA calculations.

moval of protons from the  $1p$ -shell of  $^{16}\text{O}$  as a function of  $p_{\text{miss}}$ . Note that the data point located at  $p_{\text{miss}}\approx 52$  MeV/ $c$  comes from the parallel kinematics measurements,<sup>13</sup> while the other data points come from the quasiperpendicular kinematics measurements. The solid line is the RDWIA calculation, while the dashed and dashed-dotted lines are, respectively, the bare ROMEA and RMSGA calculations. The agreement, particularly between the RDWIA calculations and the data, is very good. The spinor distortions in the RDWIA calculations which were required to predict the change in slope of  $A_{LT}$  at  $p_{\text{miss}}\approx 300$  MeV/ $c$  in Fig. 12 are also essential to the description of  $R_{LT}$ . The agreement between the RMSGA calculations and the data, particularly for  $R_{LT}$ , is markedly poorer.

Qualitatively, it should again be noted that none of the calculations presented so far have included contributions from two-body currents. The good agreement between the calculations and the data indicates that these currents are already small at  $Q^2\approx 0.8$  (GeV/ $c$ )<sup>2</sup>. This observation is supported by independent calculations by Amaro *et al.* [105,106] which estimate the importance of such currents (which are highly dependent on  $p_{\text{miss}}$ ) to be large at lower  $Q^2$ , but only 2% for the  $1p_{1/2}$ -state and 8% for the  $1p_{3/2}$ -state in these kinematics. It should also be noted that the RDWIA results presented here are comparable with those obtained in

<sup>13</sup>Strictly speaking, the effective longitudinal response function  $R_L$  could not be separated from the quasiperpendicular kinematics data. However, since both Kelly and Udías *et al.* calculate the term  $(v_{TT}/v_L)R_{TT}$  to be  $<10\%$  of  $R_{L+TT}$  in these kinematics,  $R_L$  and  $R_{L+TT}$  responses are both presented on the same plot.



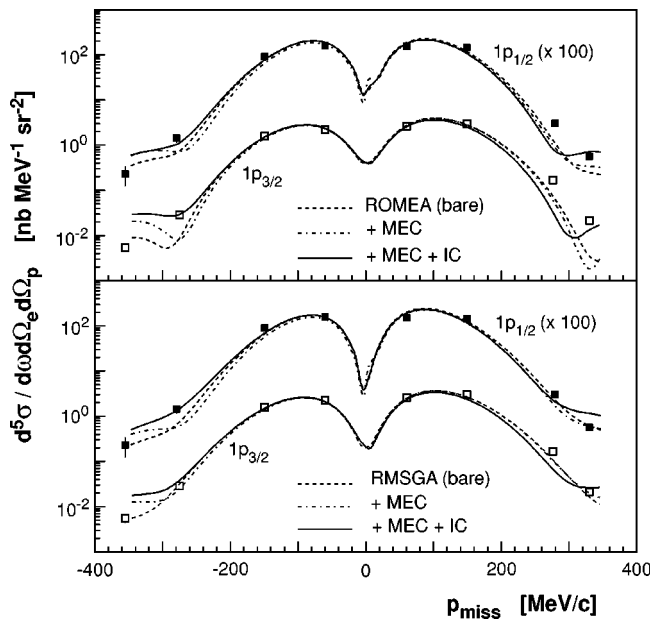


FIG. 17. Measured cross-section data for the removal of protons from the  $1p$ -shell of  $^{16}\text{O}$  as a function of  $p_{\text{miss}}$  together with calculations by the Ghent Group at  $E_{\text{beam}}=2.442$  GeV. Uncertainties are statistical and, on average, there is an additional  $\pm 5.6\%$  systematic uncertainty. The curves labeled “bare” are identical to those shown in Fig. 14.

independent RDWIA analyses of our data by the Pavia Group—see Meucci *et al.* [81].

### 3. Comparison to ROMEA and RMSGA calculations including two-body currents

In this section, two-body current contributions to the ROMEA and RMSGA calculations stemming from MEC and IC are presented. These contributions to the transition matrix elements were determined within the nonrelativistic framework outlined by the Ghent Group in Ref. [107]. Recall that the basic options employed in the calculations have been summarized in Table VIII. Note again that both the EA-based calculations stop at  $p_{\text{miss}}=350$  MeV/ $c$  as the approximation becomes invalid.

Figure 17 shows measured cross-section data for the removal of protons from the  $1p$ -shell of  $^{16}\text{O}$  as a function of  $p_{\text{miss}}$  as compared to calculations by the Ghent Group which include MEC and IC at  $E_{\text{beam}}=2.442$  GeV. In the top panel, ROMEA calculations are shown. The dashed line is the bare calculation, the dashed-dotted line includes MEC, and the solid line includes both MEC and IC. In the bottom panel, RMSGA calculations are shown. The dashed line is the bare calculation, the dashed-dotted line includes MEC, and the solid line includes both MEC and IC. Note that the curves labeled “bare” in this figure are identical to those shown in Fig. 14. The normalization factors are 0.6 and 0.7 for the  $1p_{1/2}$ -state and  $1p_{3/2}$ -state, respectively. The impact of the two-body currents on the computed differential cross section for the knockout of  $1p$ -shell protons from  $^{16}\text{O}$  is no more than a few percent for low  $p_{\text{miss}}$ , but gradually increases with increasing  $p_{\text{miss}}$ . Surprisingly, the explicit inclusion of the

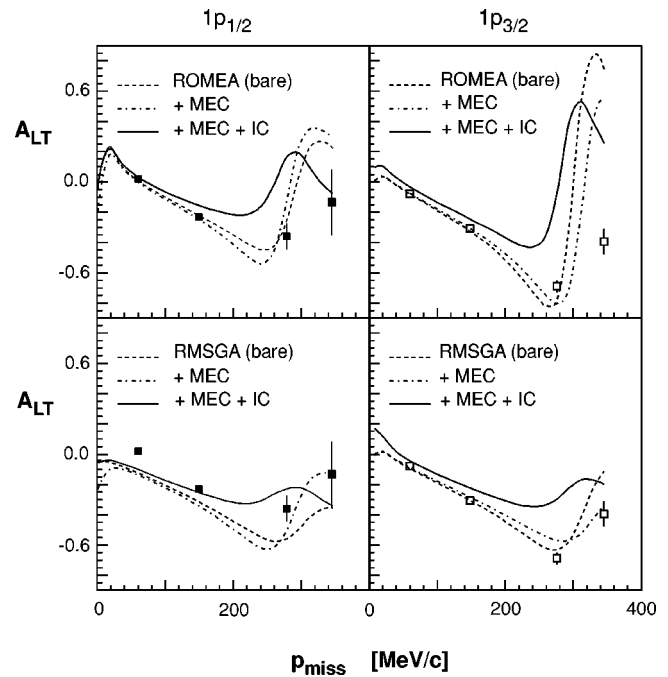


FIG. 18. Left-right asymmetry  $A_{LT}$  together with calculations by the Ghent Group of the  $A_{LT}$  asymmetry for the removal of protons from the  $1p$ -shell of  $^{16}\text{O}$  as a function of  $p_{\text{miss}}$  for  $E_{\text{beam}}=2.442$  GeV. Error bars are statistical. The curves labeled “bare” are identical to those shown in Fig. 15.

two-body current contributions to the transition matrix elements does not markedly improve the overall agreement between the calculations and the data.

Figure 18 shows the left-right asymmetry  $A_{LT}$  together with calculations by the Ghent Group for the removal of protons from the  $1p$ -shell of  $^{16}\text{O}$  as a function of  $p_{\text{miss}}$  for  $E_{\text{beam}}=2.442$  GeV. In the top two panels, ROMEA calculations are shown. The dashed lines are the bare calculations identical to those previously shown in Fig. 15, the dashed-dotted line includes MEC, and the solid line includes both MEC and IC. In the bottom panel, RMSGA calculations are shown. The dashed line is the bare calculation, the dashed-dotted line includes MEC, and the solid line includes both MEC and IC. While all three calculations undergo a change in slope at  $p_{\text{miss}}\approx 300$  MeV/ $c$ , it is again clearly the bare calculations which best represent the data. Note that in general, the IC were observed to produce larger effects than the MEC.

Figures 19 and 20 show the effective  $R_{L+TT}$ ,  $R_{LT}$ , and  $R_T$  response functions together with ROMEA and RMSGA calculations by the Ghent Group for the removal of protons from the  $1p$ -shell of  $^{16}\text{O}$  as a function of  $p_{\text{miss}}$ . The dashed lines are the bare ROMEA and RMSGA calculations identical to those previously shown in Fig. 16, while the solid lines include both MEC and IC. In contrast to the cross-section (recall Fig. 17) and  $A_{LT}$  (recall Fig. 18) situations, the agreement between the effective response-function data and the calculations improves with the explicit inclusion of the two-body current contributions to the transition matrix elements.

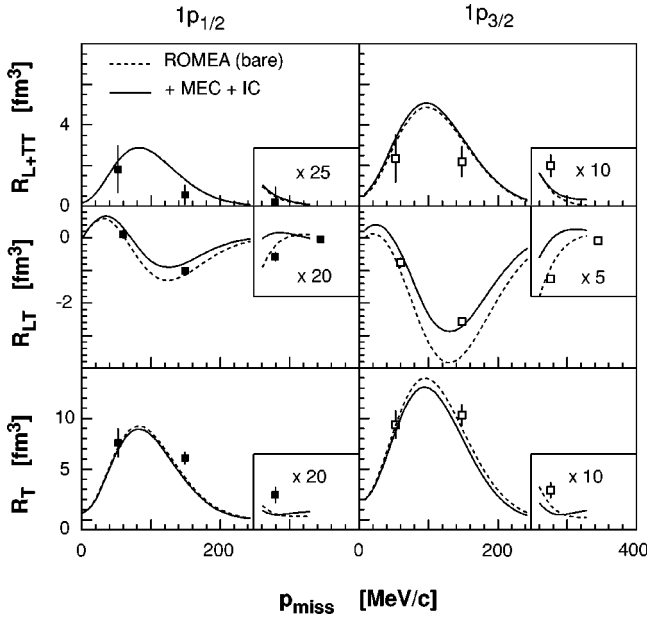


FIG. 19. Data from this work together with ROMEA calculations by the Ghent Group for the  $R_{L+TT}$ ,  $R_{LT}$ , and  $R_T$  effective response functions for the removal of protons from the  $1p$ -shell of  $^{16}\text{O}$  as a function of  $p_{\text{miss}}$ . Uncertainties are statistical. The curves labeled “bare” are identical to those shown in Fig. 16.

### B. Higher missing energies

In this section, ROMEA calculations are compared to the higher- $E_{\text{miss}}$  data. The basic options employed in the calculations have been summarized in Table VIII.

Figure 21 presents averaged measured cross-section data as a function of  $E_{\text{miss}}$  obtained at  $E_{\text{beam}}=2.442$  GeV for

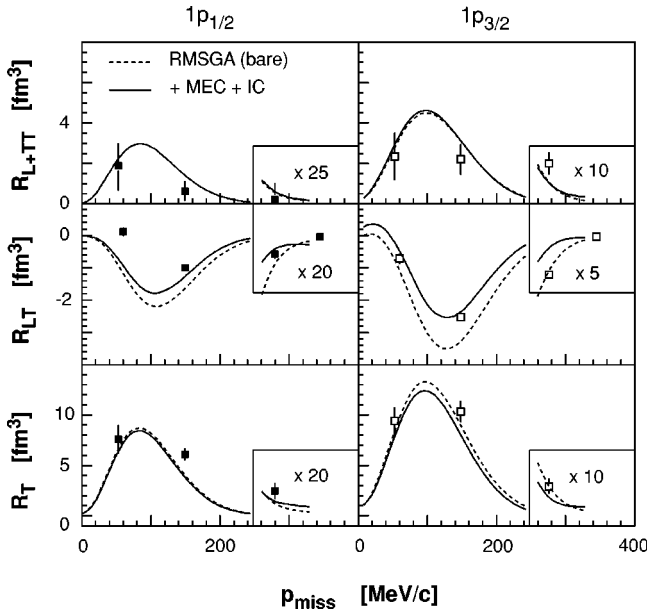


FIG. 20. Data from this work together with RMSGa calculation by the Ghent Group for the  $R_{L+TT}$ ,  $R_{LT}$ , and  $R_T$  effective response functions for the removal of protons from the  $1p$ -shell of  $^{16}\text{O}$  as a function of  $p_{\text{miss}}$ . Uncertainties are statistical. The curves labeled “bare” are identical to those shown in Fig. 16.

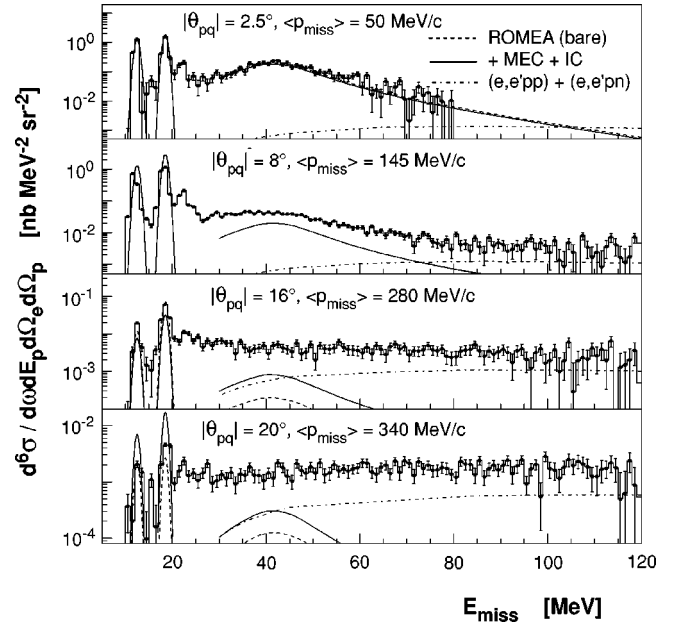


FIG. 21. Data from this work together with ROMEA calculations by the Ghent Group for the  $E_{\text{miss}}$ -dependence of the cross section obtained at  $E_{\text{beam}}=2.442$  GeV. The data are the averaged cross section measured on either side of  $\mathbf{q}$  at each  $\theta_{pq}$ . Normalization factors of 0.6, 0.7, and 1.0 have been used for the  $1p_{1/2}$ -,  $1p_{3/2}$ -, and  $1s_{1/2}$ -states, respectively. Uncertainties are statistical and, on average, there is an additional  $\pm 5.9\%$  systematic uncertainty associated with the data. Also shown are calculations by the Ghent Group for the  $(e, e'pN)$  contribution.

four discrete HRS<sub>h</sub> angular settings ranging from  $2.5^\circ < \theta_{pq} < 20^\circ$ , corresponding to average values of  $p_{\text{miss}}$  increasing from 50 to 340 MeV/c. The cross-section values shown are the averaged values of the cross section measured on either side of  $\mathbf{q}$  at each  $\theta_{pq}$ . The strong peaks at  $E_{\text{miss}} = 12.1$  and 18.3 MeV correspond to  $1p$ -shell proton removal from  $^{16}\text{O}$ . As in Sec. V A, the dashed curves corresponding to these peaks are the bare ROMEA calculations, while the solid lines include both MEC and IC. The normalization factors remain 0.6 and 0.7 for the  $1p_{1/2}$ - and  $1p_{3/2}$ -states, respectively.

For  $20 < E_{\text{miss}} < 30$  MeV, the spectra behave in a completely different fashion. Appreciable strength exists which scales roughly with the  $1p$ -shell fragments and is not addressed by the present calculations of two-nucleon knockout. The high-resolution experiment of Leuschner *et al.* identified two additional  $1p_{3/2}$ -fragments and several positive-parity states in this region which are populated primarily by single-proton knockout from  $2p2h$  components of the ground-state wave function. Two-body currents and channel-coupling in the final state also contribute. This strength has also been studied in  $(\gamma, p)$  experiments, and has been interpreted by the Ghent Group [108] as the post-photoabsorption population of states with a predominant  $1p2h$  character via two-body currents.

For  $E_{\text{miss}} > 30$  MeV, in the top panel for  $p_{\text{miss}} = 50$  MeV/c, there is a broad and prominent peak centered at  $E_{\text{miss}} \approx 40$  MeV corresponding largely to the knockout of  $1s_{1/2}$ -state protons. As can be seen in the lower panels, the

strength of this peak diminishes with increasing  $p_{\text{miss}}$ , and completely vanishes beneath a flat background by  $p_{\text{miss}} = 280 \text{ MeV}/c$ . For  $E_{\text{miss}} > 60 \text{ MeV}$  and  $p_{\text{miss}} \geq 280 \text{ MeV}/c$ , the cross section decreases only very weakly as a function of  $p_{\text{miss}}$ , and is completely independent of  $E_{\text{miss}}$ .

In order to estimate the amount of the cross section observed for  $E_{\text{miss}} > 25 \text{ MeV}$  that can be explained by the single-particle knockout of protons from the  $1s_{1/2}$ -state, the data were compared to the ROMEA calculations of the Ghent Group. The dashed curves are the bare calculations, while the solid lines include both MEC and IC. A normalization factor of 1.0 for the  $1s_{1/2}$ -state single-particle strength was used. The two calculations are indistinguishable for  $p_{\text{miss}} \leq 145 \text{ MeV}/c$ , and the agreement between these calculations and the measured cross-section data is reasonable (see the top two panels of Fig. 21 where there is an identifiable  $1s_{1/2}$ -state peak at  $E_{\text{miss}} \approx 40 \text{ MeV}$ ). At higher  $p_{\text{miss}}$  (where there is no clear  $1s_{1/2}$ -state peak at  $E_{\text{miss}} \approx 40 \text{ MeV}$ ), the data are substantially larger than the calculated bare cross section. The inclusion of MEC and IC improves the agreement, but there is still roughly an order-of-magnitude discrepancy. The RDWIA calculations demonstrate similar behavior. Thus, the  $p_{\text{miss}} \geq 280 \text{ MeV}/c$  data are not dominated by single-particle knockout. Note that the magnitude of  $(S_T - S_L)$  is consistent with that anticipated based on the measurements of Ulmer *et al.* at  $Q^2 = 0.14 (\text{GeV}/c)^2$  and Dutta *et al.* at  $Q^2 = 0.6$  and  $1.8 (\text{GeV}/c)^2$ . Together, these data suggest that transverse processes associated with the knockout of more than one nucleon decrease with increasing  $Q^2$ .

Also shown as dashed-dotted curves in Fig. 21 are the calculations by the Ghent Group [109] for the  $(e, e'pp)$  and  $(e, e'pn)$  contributions to the  $(e, e'p)$  cross section performed within a Hartree-Fock framework. This two-particle knockout cross section was determined using the Spectator Approximation, in a calculation which included MEC, IC, and both central short-range correlations (SRC) and tensor medium-range correlations. Note that in these kinematics, this calculation performed with SRC alone produced only 2% of the two-particle knockout cross section, while including both SRC and tensor correlations produced only 15% of the two-particle knockout cross section. The calculated two-particle knockout cross section is essentially transverse in nature, since the two-body currents are predominantly transverse. The calculated strength underestimates the measured cross section by about 50% but has the observed flat shape for  $E_{\text{miss}} > 50 \text{ MeV}$ . It is thus possible that heavier meson exchange and processes involving three (or more) nucleons could provide a complete description of the data.

The measured effective response functions  $R_{L+TT}$ ,  $R_{LT}$ , and  $R_T$  together with ROMEA calculations for  $p_{\text{miss}} = 145 \text{ MeV}/c$  and  $p_{\text{miss}} = 280 \text{ MeV}/c$  are presented in Fig. 22. Kinematic overlap restricted separations to  $E_{\text{miss}} < 60 \text{ MeV}$ . The dashed curves are the bare ROMEA calculations, while the solid curves include both MEC and IC. Also shown as dashed-dotted curves are the incoherent sum of these “full” calculations and the computed  $(e, e'pN)$  contribution. In general, the data do not show the broad peak centered at  $E_{\text{miss}} \approx 40 \text{ MeV}$  corresponding to the knockout of  $1s_{1/2}$ -state protons predicted by the calculations. At  $p_{\text{miss}}$

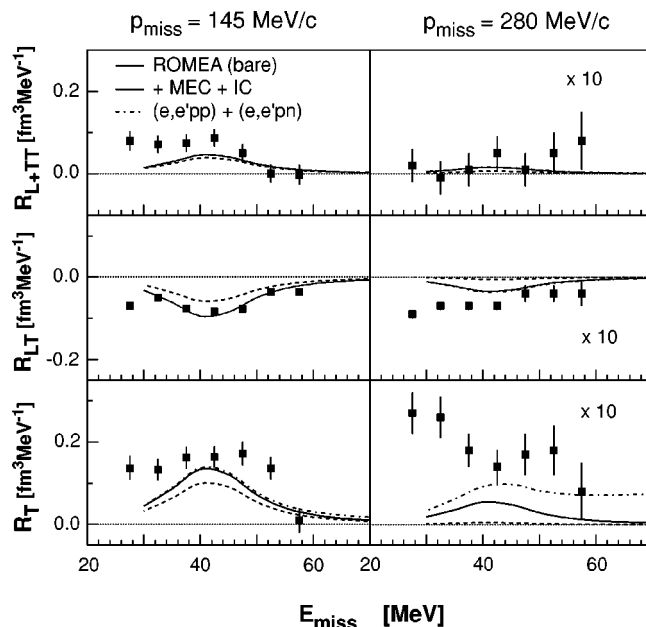


FIG. 22. Data from this work together with ROMEA calculations by the Ghent Group for the  $E_{\text{miss}}$ -dependence of the  $R_{L+TT}$ ,  $R_{LT}$ , and  $R_T$  effective response functions. Uncertainties are statistical. Also shown is the  $(e, e'pN)$  contribution.

$= 145 \text{ MeV}/c$ , the bare calculation is consistently about 60% of the magnitude of the data. The inclusion of MEC and IC does not appreciably change the calculated  $R_{L+TT}$ , but does improve the agreement between data and calculation for  $R_{LT}$  and  $R_T$ . The measured response  $R_{L+TT}$  (which is essentially equal to  $R_L$  since  $(v_{TT}/v_L)R_{TT}$  is roughly 7% of  $R_L$  in these kinematics—see Ref. [80]) is larger than the calculation for  $E_{\text{miss}} < 50 \text{ MeV}$  and smaller than the calculation for  $E_{\text{miss}} > 50 \text{ MeV}$ . The agreement between the calculation and the data for  $R_{LT}$  is very good over the entire  $E_{\text{miss}}$  range. Since the measured response  $R_{LT}$  is nonzero for  $E_{\text{miss}} > 50 \text{ MeV}$ , the measured response  $R_L$  must also be nonzero. The measured response  $R_T$  is somewhat larger than the calculation for  $E_{\text{miss}} < 60 \text{ MeV}$ .

At  $p_{\text{miss}} = 280 \text{ MeV}/c$ , the bare calculation does not reproduce the  $E_{\text{miss}}$ -dependence of any of the measured effective response functions. The inclusion of MEC and IC in the calculation substantially increases the magnitude of all three calculated response functions, and thus improves the agreement between data and calculation. The measured  $R_{L+TT}$  (which is dominated by  $R_L$ ) is consistent with both the calculation and with zero. The measured  $R_{LT}$  is about twice the magnitude of the calculation. Since the measured  $R_{LT}$  is nonzero over the entire  $E_{\text{miss}}$  range, the measured  $R_L$  must also be nonzero. The measured  $R_T$  is significantly larger than both the calculations and nonzero out to at least  $E_{\text{miss}} \approx 60 \text{ MeV}$ . The fact that the measured  $R_T$  is much larger than the measured  $R_L$  indicates the cross section is largely due to transverse two-body currents. And finally, it is clear that  $(e, e'pN)$  accounts for a fraction of the measured transverse strength which increases dramatically with increasing  $p_{\text{miss}}$ .

Figure 23 shows the calculations by the Ghent Group [89] of the contribution to the differential  $^{16}\text{O}(e, e'p)$  cross sec-

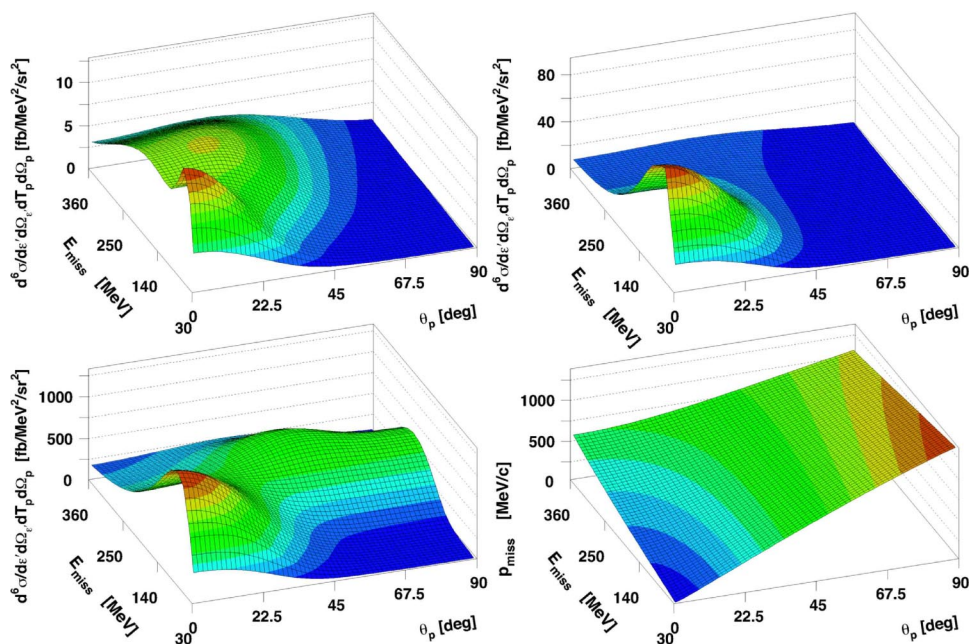


FIG. 23. (Color online) Calculations by the Ghent Group of the contribution to the differential  $^{16}\text{O}(e, e'p)$  cross section from two-nucleon knockout as a function of  $E_{\text{miss}}$  and  $\theta_p$  for  $E_{\text{beam}}=2.442$  GeV. The upper-left panel shows the contribution of central correlations. The upper-right panel shows the combined contribution of central and tensor correlations. The lower-left panel shows the combined contribution of central and tensor correlations (two-nucleon correlations) together with MEC and IC (two-body currents). The relationship between the various kinematic quantities is shown in the bottom-right panel.

tion from two-nucleon knockout as a function of  $E_{\text{miss}}$  and  $\theta_p$  for  $E_{\text{beam}}=2.442$  GeV. The upper-left panel shows the contribution of central correlations. The upper-right panel shows the combined contribution of central and tensor correlations. Tensor correlations are anticipated to dominate central correlations over the ranges of  $E_{\text{miss}}$  and  $p_{\text{miss}}$  investigated in this work. The lower-left panel shows the combined contribution of central and tensor correlations (two-nucleon correlations) together with MEC and IC (two-body currents). Two-body currents are anticipated to dominate two-nucleon correlations over the ranges of  $E_{\text{miss}}$  and  $p_{\text{miss}}$  investigated in this work. For convenience, the variation of  $p_{\text{miss}}$  with  $E_{\text{miss}}$  and  $\theta_p$  is shown in the bottom-right panel.

## VI. KINEMATIC CONSISTENCY OF $1p$ -SHELL NORMALIZATION FACTORS

There has been longstanding discussion regarding the reliability of the spectroscopic factors determined for discrete states from single-nucleon electromagnetic knockout. Recently, there has been speculation that these factors might appear to increase with  $Q^2$  as a quasiparticle state is probed with finer resolution. In this section, Kelly [110] has used the RDWIA to analyze the normalization factors fitted to the available  $^{16}\text{O}(e, e'p)$  data for the  $1p_{1/2}$ - and  $1p_{3/2}$ -states obtained in the experiments summarized in Table IX. If the RDWIA model is accurate, these factors should be independent of the experimental kinematics.

TABLE IX. A summary of the kinematic conditions for the data examined in the  $^{16}\text{O}(e, e'p)$  consistency study.

Label	Authors	Kinematics	$T_p$ (MeV)	$Q^2$ (GeV <sup>2</sup> )	$x$	$2s_{1/2}1d_{5/2}$ -doublet	Data
a	Leuschner <i>et al.</i> [14]	Parallel	96	Varied	Varied	Resolved	Reduced $\sigma$
b	Spaltro <i>et al.</i> [13]	Perpendicular	84	0.20	1.07	Resolved	Differential $\sigma$
c	Chinitz <i>et al.</i> [12]	Perpendicular	160	0.30	0.91	Computed <sup>a</sup>	Differential $\sigma$
d	this work	Perpendicular	427	0.80	0.96	Computed <sup>b</sup>	Differential $\sigma$
e	Bernheim <i>et al.</i> [11]	Perpendicular	100	0.19	0.90	Computed <sup>b</sup>	Reduced $\sigma$
f	Blomqvist1 <i>et al.</i> [15]	Parallel	92	0.08	0.30–0.50	Resolved	Reduced $\sigma$
g	Blomqvist2 <i>et al.</i> [15]	Highly varied	215	0.04–0.26	0.07–0.70	Resolved	Reduced $\sigma$

<sup>a</sup>The  $1p_{3/2}$ -state data were corrected for the contamination of the  $1d_{5/2}2s_{1/2}$ -doublet by Chinitz *et al.*

<sup>b</sup>The contamination of the  $1p_{3/2}$ -state by the  $1d_{5/2}2s_{1/2}$ -doublet was computed according to the method outlined in Sec. V A 1.



TABLE X. Normalization factors deduced for the data sets presented in Table IX for  $p_{\text{miss}} < 200$  MeV/c. The first term in each column is for the  $1p_{1/2}$ -state, while the second term is for the  $1p_{3/2}$ -state.

	HS			EDAI-O			NLSH-P			HS			EDAD1			NLSH-P							
	$S_\alpha$	$\chi^2$	$S_\alpha$	$S_\alpha$	$\chi^2$	$S_\alpha$	$S_\alpha$	$\chi^2$	$S_\alpha$	$\chi^2$	$S_\alpha$	$S_\alpha$	$\chi^2$	$S_\alpha$	$\chi^2$	$S_\alpha$	$\chi^2$						
a	0.55	0.46	0.9	4.2	0.47	2.5	6.0	0.53	0.41	1.0	1.5	0.60	0.55	0.8	2.4	0.66	0.56	2.3	3.7	0.57	0.48	0.8	1.4
b	0.61	0.66	2.7	6.3	0.68	5.4	8.0	0.58	0.58	2.3	3.6	0.71	0.75	2.3	5.1	0.77	0.77	4.2	6.4	0.68	0.65	2.2	4.1
c	0.54	0.56	8.7	17.9	0.58	24.8	25.3	0.51	0.47	9.0	15.0	0.59	0.61	8.0	18.2	0.66	0.63	16.7	22.1	0.56	0.50	7.2	23.8
d	0.62	0.63	30.8	4.7	0.70	0.5	6.7	0.59	0.52	19.6	15.3	0.62	0.63	32.5	2.4	0.70	0.66	1.2	3.9	0.60	0.53	20.0	14.4
e	0.43	0.46	1.0	1.9	0.48	0.47	2.2	0.42	0.40	1.0	1.1	0.48	0.52	1.0	1.5	0.54	0.54	1.5	1.9	0.47	0.45	1.0	1.3
f	0.53	0.41	3.0	4.2	0.54	0.42	5.0	0.51	0.38	2.7	1.9	0.57	0.50	3.2	3.7	0.59	0.51	5.8	5.0	0.54	0.46	2.7	2.1
g	0.42	0.37	2.0	1.4	0.44	0.37	4.7	0.40	0.33	2.5	5.9	0.42	0.40	1.8	1.9	0.44	0.41	6.6	2.8	0.40	0.36	1.9	5.4

### A. RDWIA analysis of the available $^{16}\text{O}(e, e'p)$ data

The RDWIA calculations used in this procedure employed the  $\bar{\Gamma}_2$  off-shell single-nucleon current operator with the MMD form factors of Mergell *et al.* [111] in the Coulomb gauge. The partial-wave expansions were performed using the second-order Dirac equation, including spinor distortion. Nucleon distortion was evaluated using the EDAD1-O and EDAD1 optical potentials, and electron distortion was evaluated in the “ $q_{\text{eff}}$  Approximation” (see Appendix A 1). No attempt to directly fit the overlap functions to the knockout data has been made here. Instead, the recently developed wave functions HS, NLSH, and NLSH-P (recall Fig. 11) were again tested, this time to see if they could satisfactorily reproduce the experimental  $p_{\text{miss}}$  distributions independently of  $Q^2$ .

The results are expressed in terms of normalization factors which compare a RDWIA calculation for a fully occupied subshell with experimental data and are presented in Table X. These factors were obtained by least-squares fitting to the data in the range  $p_{\text{miss}} < 200$  MeV/c where the RDWIA should be most reliable. When experimentally unresolved, the contamination of the  $1p_{3/2}$ -state by the  $1d_{5/2}2s_{1/2}$ -doublet was included by the incoherent summation of the parametrizations of Leuschner *et al.* as previously described.

The data sets demonstrated a slight preference for the EDAD1 optical potential over the EDAD1-O optical potential. This was concluded based on the quality of the fits and the more consistent nature of the extracted normalization factors for low  $Q^2$ . None of the variations considered in Table X (nor any of those considered in Table VII for that matter) were able to reproduce the  $1p_{3/2}$ -state for data set (b) in the range  $50 < p_{\text{miss}} < 120$  MeV/c. This problem is also responsible for the discrepancy seen in Fig. 1 for  $R_{LT}$  at  $Q^2 = 0.2$  (GeV/c) $^2$ , and has not yet been explained satisfactorily.

Unfortunately, none of the selected wave functions provided an optimal description of the experimental  $p_{\text{miss}}$  distributions independent of  $Q^2$ . Figure 24 shows a sample set of fits to the various  $^{16}\text{O}(e, e'p)$  data sets based on the HS bound-nucleon wave function and the EDAD1 optical potential.

From a  $\chi^2$  perspective, it is clear that HS offered the best description of the data at  $Q^2 = 0.8$  (GeV/c) $^2$ , but that most of the lower  $Q^2$  data are best described by either NLSH-P or HS; in fact, HS may be the best compromise currently available. Data set (g) from Mainz suggested a substantially different normalization.

An estimate of the uncertainty in the normalization factors due to variations of the bound-nucleon wave function was made by comparing NLSH/HS and NLSH-P/HS normalization-factor ratios for each state holding the optical potential and other model input constant. For the lowest-lying  $1p_{1/2}$ - and  $1p_{3/2}$ -states and averaged over all data sets, NLSH/HS ratios of 1.08 and 1.02 were obtained. Similarly, NLSH-P/HS ratios of 0.96 and 0.87 were obtained. These ratios are qualitatively consistent with the behavior of the data and the calculations near the peaks of the momentum distributions shown in Fig. 11. Therefore, a cautious estimate

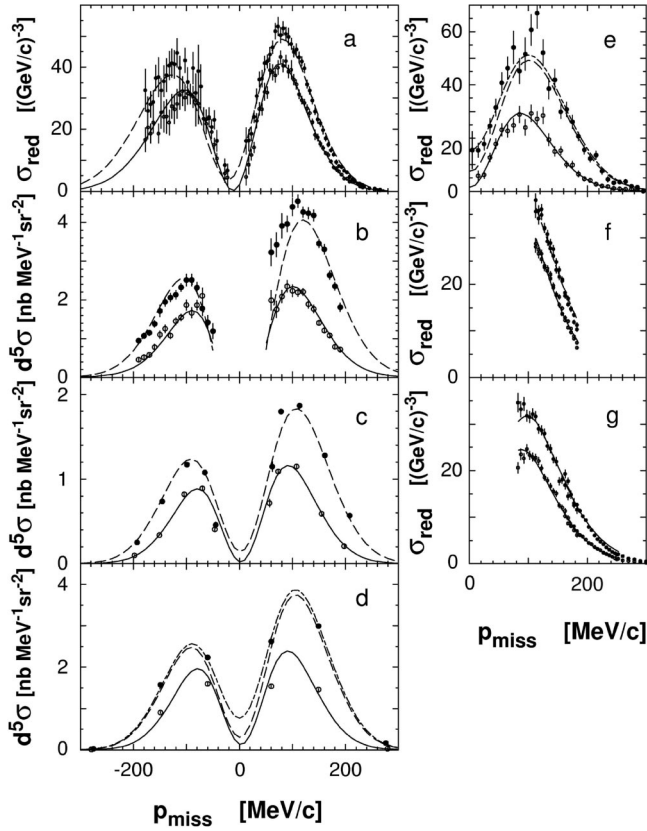


FIG. 24. Fits to various  $^{16}\text{O}(e, e'p)$  data sets based on the HS bound-nucleon wave function and the EDAD1 optical potential. See Table IX for the key to the dataset labels. Open points and solid lines pertain to the  $1p_{1/2}$ -state, while points and dashed lines pertain to the  $1p_{3/2}$ -state. The dashed-dotted lines include the contributions of the positive parity  $2s_{1/2}1d_{5/2}$ -doublet to the  $1p_{3/2}$ -state. Panel (d) shows the data from this work.

of the uncertainty due to the bound-nucleon wave function is of order  $\pm 10\%$ . Further, by changing the optical potentials between EDAD1-O and EDAD1 and holding the bound-nucleon wave function and other model input constant, EDAD1-O/EDAD1 normalization-factor ratios for a given data set with  $Q^2 < 0.4$   $(\text{GeV}/c)^2$  averaged to about 0.90. This ratio became 0.98 at  $Q^2 = 0.8$   $(\text{GeV}/c)^2$ , where the attenuation in the potentials is practically identical. Therefore, the uncertainty due to variations of the optical potential is at least  $\pm 5\%$  and would probably be larger if the sample of “reasonable” potentials were expanded.

The information presented in Table VII suggests that there would be similar uncertainties in the normalization factors for the  $Q^2 = 0.8$   $(\text{GeV}/c)^2$  data arising from Gordon and gauge ambiguities in the single-nucleon current operator. Note that values of  $S_\alpha$  for the same model are generally larger in Table VII than in Table X because the former summarizes a study of the entire  $p_{\text{miss}}$  range while the latter is limited to  $p_{\text{miss}} < 200$   $\text{MeV}/c$ , where the reaction model is likely to be most accurate. Data for larger  $p_{\text{miss}}$  also tend to have a higher  $\chi^2$ . These problems for large  $p_{\text{miss}}$  may arise from inaccuracies in the bound-nucleon wave functions

above the Fermi momentum, neglecting two-body currents, neglecting channel coupling in the final state, or density dependence in the form factors, to name a few. Therefore, a realistic estimate of the model dependence of the normalization factors for  $(e, e'p)$  reactions should not be less than  $\pm 15\%$ . This estimated precision is consistent with that suggested in Ref. [2]—although the relativistic model improves our description of  $A_{LT}$ , recoil polarization, and other normalization-independent features of the reaction, the model dependencies that affect the normalization uncertainty are not significantly improved. Assuming that the reaction model is most reliable at large  $Q^2$  and modest  $p_{\text{miss}}$ , the six  $1p_{1/2}$ - and  $1p_{3/2}$ -state normalization factors for data set (d) in Table X (this work) were averaged to conclude that the normalization factors for the lowest  $1p_{1/2}$ - and  $1p_{3/2}$ -states in  $^{15}\text{N}$  are approximately 0.63(9) and 0.60(9).

As previously mentioned, Leuschner *et al.* identified two additional  $1p_{3/2}$ -states with excitation energies between 9 and 13 MeV that together carry approximately 11% of the strength of the lowest-energy fragment. However, those states were not resolved by the present experiment. If the assumption is made that the same ratio applies at  $Q^2 \approx 0.8$   $(\text{GeV}/c)^2$ , then the total  $1p_{3/2}$  strength below 15 MeV excitation is estimated to be approximately 67% of full occupancy, and the total  $1p$ -shell spectroscopic strength below 15 MeV represents  $3.9 \pm 0.6$  protons or about 65% of full occupancy. This result remains 10–20% below predictions from recent calculations of the hole spectral function by Barbieri and Dickhoff [112], but no experimental estimate for the additional  $1p$ -shell strength that might lurk beneath the continuum is available.

To obtain more precise normalization factors, it would be necessary to apply a relativistic analysis to data in quasiperpendicular kinematics for several values of  $Q^2$  larger than about 0.5  $(\text{GeV}/c)^2$  and with sufficient coverage of the  $p_{\text{miss}}$  distribution to fit the bound-nucleon wave function requiring that it be independent of  $Q^2$ . Although such data do not yet exist for  $^{16}\text{O}$ , the recently completed experiment in Hall A at Jefferson Lab will provide substantially more data points for the critical  $p_{\text{miss}} < 200$   $\text{MeV}/c$  region for  $Q^2 = 0.9$   $(\text{GeV}/c)^2$ .

## B. $Q^2$ -dependence of normalization factors

Lapikás *et al.* [113] have performed a similar type of analysis of the  $Q^2$ -dependence of the normalization factors for the  $^{12}\text{C}(e, e'p)$  reaction. In their work, several data sets with  $Q^2 < 0.3$   $(\text{GeV}/c)^2$  were analyzed using a nonrelativistic DWIA model. For each data set, a normalization factor and the radius parameter for a Woods-Saxon binding potential were fitted to the reduced cross section for discrete states, and the potential depths were adjusted to fit the separation energies. Consistent normalization factors were obtained for all data sets save those measured by Blomqvist *et al.* at Mainz [114]. A new experiment was thus performed at NIKHEF duplicating the Mainz kinematics. The new results were also consistent with all data sets save those from Mainz. Lapikás *et al.* thus concluded that the Mainz data

were normalized incorrectly.<sup>14</sup> After excluding the Mainz data, Lapikás *et al.* determined that the summed  $1p$ -shell strength for  $^{12}\text{C}$  could in fact be deduced from data for  $Q^2 < 0.3 (\text{GeV}/c)^2$  with an uncertainty of  $\pm 3\%$ . However, they did not consider the effects of variations of the optical model or several other uncertain aspects of the reaction model. As discussed previously, a more realistic estimate of the relative uncertainty in the normalization factors must be closer to  $\pm 15\%$  due to the inevitable model dependence of the DWIA. Furthermore, it is possible that variation of the Woods-Saxon radius might affect the resulting normalization factors. If the overlap function is an intrinsic property of the nuclear wave function, it should not depend upon  $Q^2$ . Further, it should be possible to fit a common radius to all data simultaneously; if not, the accuracy of the reaction model must be questioned. And of course, it has been demonstrated in recent years that a relativistic DWIA model is preferable to a nonrelativistic approach.

Lapikás *et al.* also used the bound-nucleon wave functions and normalization factors obtained from their nonrelativistic analysis at low  $Q^2$  to analyze the transparency of  $^{12}\text{C}$  for  $Q^2$  up to  $7 (\text{GeV}/c)^2$  and the summed  $1p$ - and  $1s$ -shell spectroscopic amplitude. They found the summed spectroscopic strength was approximately constant at 0.58 for  $Q^2 \leq 0.6 (\text{GeV}/c)^2$ , but rose for larger  $Q^2$  and appeared to approach the Independent-Particle Model limit of unity somewhere near  $Q^2 \approx 10 (\text{GeV}/c)^2$ . They speculated that the apparent  $Q^2$ -dependence of this spectroscopic strength might be related to the resolution at which a quasiparticle is probed, with long-range correlations that deplete the single-particle strength becoming less important at higher  $Q^2$  and finer resolution. A subsequent analysis by Frankfurt *et al.* using Glauber calculations for heavier targets [115] supports this interpretation.

Little evidence is seen here for a systematic dependence in the normalization factors upon either  $T_p$  or  $Q^2$  for the lowest  $1p$ -states of  $^{16}\text{O}$  for the data that are presently available. Unfortunately, these data do not reach high enough  $Q^2$  to address the resolution hypothesis. Furthermore, the normalization factors for two of the data sets appear to be anomalously low. A normalization problem might not be too surprising for data set (e) because it comes from one of the earliest experiments on this reaction, but data set (g) comes from a fairly recent experiment at Mainz and uses an ejectile energy large enough for the reaction model to be reliable. As discussed above for the case of  $^{12}\text{C}$ , it is likely that data set (g) also has a normalization error.<sup>15</sup> If these two data sets are disregarded, the remaining low  $Q^2$  data are consistent with the normalization factors deduced from the current  $Q^2 \approx 0.8 (\text{GeV}/c)^2$  data.

<sup>14</sup>Recall that similar doubts regarding the normalization of the companion  $^{16}\text{O}(e, e'p)$  experiment [15] at Mainz had been expressed earlier by Kelly [4], but independent data duplicating the measurement are unfortunately not available.

<sup>15</sup>Difficulties associated with the reaction mechanism relatively far from QE kinematics may also be partly responsible for the anomalously low normalization factors for these data.

## VII. SUMMARY AND CONCLUSIONS

The  $^{16}\text{O}(e, e'p)$  reaction in QE, constant  $(q, \omega)$  kinematics at  $Q^2 \approx 0.8 (\text{GeV}/c)^2$ ,  $q \approx 1 \text{ GeV}/c$ , and  $\omega \approx 445 \text{ MeV}$  was studied for  $0 < E_{\text{miss}} < 120 \text{ MeV}$  and  $0 < p_{\text{miss}} < 350 \text{ MeV}/c$ . Five-fold differential cross-section data for the removal of protons from the  $1p$ -shell were obtained for  $0 < p_{\text{miss}} < 350 \text{ MeV}/c$ . Six-fold differential cross-section data for  $0 < E_{\text{miss}} < 120 \text{ MeV}$  were obtained for  $0 < p_{\text{miss}} < 350 \text{ MeV}/c$ . These results were used to extract the  $A_{LT}$  asymmetry and the  $R_L$ ,  $R_T$ ,  $R_{L+TT}$ , and  $R_{LT}$  effective response functions over a large range of  $E_{\text{miss}}$  and  $p_{\text{miss}}$ .

The data were interpreted in subsets corresponding to the  $1p$ -shell and the  $1s_{1/2}$ -state and continuum, respectively.  $1p$ -shell data were interpreted within three fully relativistic frameworks for single-particle knockout which do not include any two-body currents: RDWIA, ROMEA, and RMSGA. Two-body current contributions to the ROMEA and RMSGA calculations for the  $1p$ -shell stemming from MEC and IC were also considered. The  $1s_{1/2}$ -state and continuum data were considered within the identical ROMEA framework both before and after two-body current contributions due MEC and IC were included.  $(e, e'pN)$  contributions to these data were also examined.

Overall, the RDWIA calculations provided by far the best description of the  $1p$ -shell data. Dynamic effects due to the inclusion of the lower components of the Dirac spinors in these calculations were necessary to self-consistently reproduce the  $1p$ -shell cross-section data, the  $A_{LT}$  asymmetry, and the  $R_{LT}$  effective response function over the entire measured range of  $p_{\text{miss}}$ . Within the RDWIA framework, the four most important ingredients were the inclusion of both bound-nucleon and ejectile spinor distortion, the choice of current operator, the choice of bound-nucleon wave function, and the choice of optical potential. An inclusion of the spinor distortion resulted in a diffractive change in slope in  $A_{LT}$  at  $p_{\text{miss}} \approx 300 \text{ MeV}/c$  which agreed nicely with the data. A different choice of current operator either damped out or magnified this change in slope. A different choice of bound-nucleon wave function changed the  $p_{\text{miss}}$ -location of the change in slope, but preserved the magnitude. A different choice of optical potential changed the magnitude of the change in slope but preserved the  $p_{\text{miss}}$ -location.

As anticipated, since  $p_p \approx 1 \text{ GeV}/c$ , the ROMEA calculations provided a reasonable description of the  $1p$ -shell data. For this energy range, optical models generally provide an overall better description of proton elastic scattering than does the Glauber model. This is in part due to important medium modifications of the  $NN$  interaction from Pauli blocking and spinor distortion. Surprisingly, the unfactorized “out-of-the-box” RMSGA calculation provided a fairly good description of the  $1p$ -shell data already at this relatively low proton momentum. Adding the contributions of two-body currents due to MEC and IC to the descriptions of the  $1p$ -shell data provided by the bare ROMEA and RMSGA calculations did not improve the agreement.

The RDWIA calculation with single-nucleon currents was used to fit normalization factors to the data from this experiment and from several other experiments at lower  $Q^2$ . Ignoring two experiments which appear to have normalization



problems, normalization factors of 0.63(9) and 0.60(9) were obtained for the lowest  $1p_{1/2}$ - and  $1p_{3/2}$ -states with no significant dependence upon  $Q^2$  or  $T_p$ . The estimated uncertainties account for variations due to the choice of bound-nucleon wave functions, optical potentials, and other aspects of the model. After accounting for other known but unresolved  $1p_{3/2}$ -states, the total  $1p$ -shell spectroscopic strength below about 15 MeV excitation is estimated to be about  $0.65 \pm 0.10$  relative to full occupancy.

For  $25 < E_{\text{miss}} < 50$  MeV and  $p_{\text{miss}} \leq 145$  MeV/ $c$ , the reaction was dominated by the knockout of  $1s_{1/2}$ -state protons and the cross section and effective response functions were reasonably well-described by bare ROMEA calculations which did not consider the contributions of two-body currents due to MEC and IC. However, as  $p_{\text{miss}}$  increased beyond 145 MeV/ $c$ , the single-particle aspect of the reaction diminished. Cross-section data and response functions were no longer peaked at  $E_{\text{miss}} \approx 40$  MeV, nor did they exhibit the Lorentzian  $s$ -shell shape. Already at  $p_{\text{miss}} = 280$  MeV/ $c$ , the same bare ROMEA calculations that did well describing the data for  $p_{\text{miss}} < 145$  MeV/ $c$  underestimated the cross-section data by more than an order of magnitude. Including the contributions of two-body currents due to MEC and IC improved the agreement for  $E_{\text{miss}} < 50$  MeV, but the calculations still dramatically underpredict the data.

For  $25 < E_{\text{miss}} < 120$  MeV and  $p_{\text{miss}} \geq 280$  MeV/ $c$ , the cross-section data were almost constant as a function of both  $p_{\text{miss}}$  and  $E_{\text{miss}}$ . Here, the single-particle aspect of the  $1s_{1/2}$ -state contributed  $< 10\%$  to the cross section. Two-nucleon ( $e, e'pN$ ) calculations accounted for only about 50% of the magnitude of the cross-section data, but reproduced the shape well. The model, which explained the shape, transverse nature, and 50% of the measured cross section, suggested that the contributions of the two-nucleon currents due to MEC and IC are much larger than those of the two-nucleon correlations. The magnitude of the measured cross section that remains unaccounted for suggests additional currents and processes play an equally important role.

#### ACKNOWLEDGMENTS

We acknowledge the outstanding support of the staff of the Accelerator and Physics Divisions at Jefferson Lab that made this experiment successful. We thank T. W. Donnelly and J. W. Van Orden for valuable discussions. This work was supported in part by the U. S. Department of Energy Contract No. DE-AC05-84ER40150 under which the Southeastern Universities Research Association (SURA) operates the Thomas Jefferson National Accelerator Facility, other Department of Energy contracts, the National Science Foundation, the Swedish Research Council (VR), the Italian Istituto Nazionale di Fisica Nucleare (INFN), the French Centre National de la Recherche Scientifique (CNRS) and Commissariat à l'Énergie Atomique, and the Natural Sciences and Engineering Research Council of Canada.

#### APPENDIX A: THEORETICAL FORMALISMS

##### 1. RDWIA

The five-fold differential cross section for the exclusive  $A(e, e'N)B$  reaction leading to a discrete final state takes the form (see Ref. [2])

$$\frac{d^5\sigma}{d\varepsilon_f d\Omega_e d\Omega_N} = K \frac{\varepsilon_f \alpha^2}{\varepsilon_i Q^4} \eta_{\mu\nu} \mathcal{W}^{\mu\nu}, \quad (\text{A1})$$

where

$$K = \mathcal{R} \frac{p_N E_N}{(2\pi)^3} \quad (\text{A2})$$

is a phase-space factor,  $k_i = (\varepsilon_i, \mathbf{k}_i)$  and  $k_f = (\varepsilon_f, \mathbf{k}_f)$  are the initial and final electron momenta,  $p_A = (E_A, \mathbf{p}_A)$  and  $p_B = (E_B, \mathbf{p}_B)$  are the initial and final target momenta,  $p_N = (E_N, \mathbf{p}_N)$  is the ejected-nucleon momentum,  $q = k_i - k_f = (\omega, \mathbf{q})$  is the momentum transfer carried by the virtual photon,  $Q^2 = -q_\mu q^\mu = \mathbf{q}^2 - \omega^2$  is the photon virtuality, and

$$\mathcal{R} = \left| 1 - \frac{\mathbf{v}_N \cdot \mathbf{v}_B}{\mathbf{v}_N \cdot \mathbf{v}_N} \right|^{-1} \quad (\text{A3})$$

(with  $v_N = p_N/E_N$ ) is a recoil factor which adjusts the nuclear phase space for the missing-energy constraint. In the OPEA, the invariant electroexcitation matrix element is represented by the contraction of electron and nuclear response tensors of the form

$$\eta_{\mu\nu} = \langle j_\mu j_\nu^\dagger \rangle, \quad (\text{A4})$$

$$\mathcal{W}_{\mu\nu} = \langle \mathcal{J}_\mu \mathcal{J}_\nu^\dagger \rangle, \quad (\text{A5})$$

where  $j^\mu$  is the electron current,  $\mathcal{J}^\mu$  is a matrix element of the nuclear electromagnetic current, and the angled brackets denote averages over initial states and sums over final states. The reduced cross section is given by

$$\sigma_{\text{red}} = \frac{d^5\sigma}{d\varepsilon_f d\Omega_e d\Omega_N} / K \sigma_{eN}, \quad (\text{A6})$$

where

$$\sigma_{eN} = \frac{\varepsilon_f \alpha^2}{\varepsilon_i Q^4} (\eta_{\mu\nu} \mathcal{W}^{\mu\nu})_{\text{PWIA}} \quad (\text{A7})$$

is the elementary cross section for electron scattering from a moving free nucleon in the Plane-Wave Impulse Approximation (PWIA). The PWIA response tensor is computed for a free nucleon in the final state, and is given by

$$W_{\text{PWIA}}^{\mu\nu} = \frac{1}{2} \text{Trace} J^\mu J^{\nu\dagger}, \quad (\text{A8})$$

where

$$J_{s_f s_i}^\mu = \sqrt{\frac{m^2}{\varepsilon_i \varepsilon_f}} \bar{u}(\mathbf{p}_f, s_f) \Gamma^\mu u(\mathbf{p}_i, s_i) \quad (\text{A9})$$

is the single-nucleon current between free spinors normalized to unit flux. The initial momentum ( $\mathbf{p}_i = \mathbf{p}_f - \mathbf{q}_{\text{eff}}$ ) is obtained from the final ejectile momentum ( $\mathbf{p}_f$ ) and the effective momentum transfer ( $\mathbf{q}_{\text{eff}}$ ) in the laboratory frame, and the initial energy is placed on shell. The effective momentum transfer accounts for electron acceleration in the nuclear Coulomb field and is discussed further later in this section.

In the nonrelativistic PWIA limit,  $\sigma_{\text{red}}$  reduces to the bound-nucleon momentum distribution, and the cross section



given in Eq. (A1) may be expressed as the product of the phase-space factor  $K$ , the elementary cross section  $\sigma_{eN}$ , and the momentum distribution. This is usually referred to “factorization”. Factorization is not strictly valid relativistically because the binding potential alters the relationship between lower and upper components of a Dirac wave function—see Ref. [116]. In this section, it is assumed that the nuclear current is represented by a one-body operator, such that

$$\mathcal{J}^\mu = \int d^3r \exp(it \cdot \mathbf{r}) \langle \bar{\Psi}^{(-)}(\mathbf{p}, \mathbf{r}) | \Gamma^\mu | \phi(\mathbf{r}) \rangle, \quad (\text{A10})$$

where  $\phi$  is the nuclear overlap for single-nucleon knockout (often described as the bound-nucleon wave function),  $\bar{\Psi}^{(-)}$  is the Dirac adjoint of the time-reversed distorted wave,  $\mathbf{p}$  is the relative momentum, and

$$\mathbf{t} = \frac{E_B}{W} \mathbf{q} \quad (\text{A11})$$

is the recoil-corrected momentum transfer in the barycentric frame. Here  $(\omega, \mathbf{q})$  and  $E_B$  are the momentum transfer and the total energy of the residual nucleus in the laboratory frame, respectively, and  $W = \sqrt{(m_A + \omega)^2 - \mathbf{q}^2}$  is the invariant mass.

De Forest [117] and Chinn and Picklesimer [118] have demonstrated that the electromagnetic vertex function for a free nucleon can be represented by any of three Gordon-equivalent operators:

$$\Gamma_1^\mu(\mathbf{p}_f, \mathbf{p}_i) = \gamma^\mu G_M(Q^2) - \frac{P^\mu}{2m} F_2(Q^2), \quad (\text{A12a})$$

$$\Gamma_2^\mu(\mathbf{p}_f, \mathbf{p}_i) = \gamma^\mu F_1(Q^2) + i\sigma^{\mu\nu} \frac{q_\nu}{2m} F_2(Q^2), \quad (\text{A12b})$$

$$\Gamma_3^\mu(\mathbf{p}_f, \mathbf{p}_i) = \frac{P^\mu}{2m} F_1(Q^2) + i\sigma^{\mu\nu} \frac{q_\nu}{2m} G_M(Q^2), \quad (\text{A12c})$$

where  $P = (E_f + E_i, \mathbf{p}_f + \mathbf{p}_i)$ . Note the correspondence with Eq. (A13) below. Although  $\Gamma_2$  is arguably the most fundamental because it is defined in terms of the Dirac and Pauli form factors  $F_1$  and  $F_2$ ,  $\Gamma_1$  is often used because the matrix elements are easier to evaluate.  $\Gamma_3$  is rarely used but no less fundamental. In all calculations presented here, the momenta in the vertex functions are evaluated using asymptotic laboratory kinematics instead of differential operators.

Unfortunately, as bound nucleons are not on shell, an off-shell extrapolation (for which no rigorous justification exists) is required. The de Forest prescription is employed, in which the energies of both the initial and the final nucleons are placed on shell based upon effective momenta, and the energy transfer is replaced by the difference between on-shell nucleon energies in the operator. Note that the form factors are still evaluated at the  $Q^2$  determined from the electron-scattering kinematics. In this manner, three prescriptions

$$\bar{\Gamma}_1^\mu = \gamma^\mu G_M(Q^2) - \frac{\bar{P}^\mu}{2m} F_2(Q^2), \quad (\text{A13a})$$

$$\bar{\Gamma}_2^\mu = \gamma^\mu F_1(Q^2) + i\sigma^{\mu\nu} \frac{\bar{q}_\nu}{2m} F_2(Q^2), \quad (\text{A13b})$$

$$\bar{\Gamma}_3^\mu = \frac{\bar{P}^\mu}{2m} F_1(Q^2) + i\sigma^{\mu\nu} \frac{\bar{q}_\nu}{2m} G_M(Q^2), \quad (\text{A13c})$$

are obtained, where

$$\bar{q} = (E_f - \bar{E}_i, \mathbf{q}),$$

$$\bar{P} = (E_f + \bar{E}_i, 2\mathbf{p}_f - \mathbf{q}),$$

and where  $\bar{E}_i = \sqrt{m_N^2 + (\mathbf{p}_f - \mathbf{q})^2}$  is placed on shell based upon the externally observable momenta  $\mathbf{p}_f$  and  $\mathbf{q}$  evaluated in the laboratory frame. When electron distortion is included, the local momentum transfer  $\mathbf{q} \rightarrow \mathbf{q}_{\text{eff}}$  is interpreted as the effective momentum transfer with Coulomb distortion. These operators are commonly named CC1, CC2, and CC3, and are no longer equivalent when the nucleons are off-shell. Furthermore, the effects of possible density dependence in the nucleon form factors can be evaluated by applying the Local Density Approximation (LDA) to Eq. (A13)—see Refs. [80,118].

The overlap function is represented as a Dirac spinor of the form

$$\phi_{\kappa m}(\mathbf{r}) = \begin{pmatrix} f_\kappa(r) \mathcal{Y}_{\kappa m}(\hat{r}) \\ i g_{-\kappa}(r) \mathcal{Y}_{-\kappa m}(\hat{r}) \end{pmatrix}, \quad (\text{A14})$$

where

$$\mathcal{Y}_{\kappa m}(\hat{r}) = \sum_{\nu, m_s} \left\langle \ell \nu \frac{1}{2} m_s | j m \right\rangle Y_{\ell \nu}(\hat{r}) \chi_{m_s}, \quad (\text{A15})$$

is the spin spherical harmonic and where the orbital and total angular momenta are, respectively, given by

$$\ell = S_\kappa \left( \kappa + \frac{1}{2} \right) - \frac{1}{2}, \quad (\text{A16a})$$

$$j = S_\kappa \kappa - \frac{1}{2}, \quad (\text{A16b})$$

with  $S_\kappa = \text{sign}(\kappa)$ . The functions  $f_\kappa$  and  $g_\kappa$  satisfy the usual coupled linear differential equations—see for example Ref. [119]. The corresponding momentum wave function

$$\tilde{\phi}_{\kappa m}(\mathbf{p}_m) = \int d^3r \exp(-i\mathbf{p}_m \cdot \mathbf{r}) \phi_{\kappa m}(\mathbf{r}) \quad (\text{A17})$$

then takes the form

$$\tilde{\phi}_{\kappa m}(\mathbf{p}_m) = 4\pi i^{-\ell} \begin{pmatrix} \tilde{f}_\kappa(p_m) \mathcal{Y}_{\kappa m}(\hat{p}_m) \\ -S_\kappa \tilde{g}_{-\kappa}(p_m) \mathcal{Y}_{-\kappa m}(\hat{p}_m) \end{pmatrix}, \quad (\text{A18})$$

where

$$\tilde{f}_\kappa(p_m) = \int dr r^2 j_\ell(p_m r) f_\kappa(r), \quad (\text{A19a})$$

$$\tilde{g}_{-\kappa}(p_m) = \int dr r^2 j_{\ell'}(p_m r) g_{-\kappa}(r), \quad (\text{A19b})$$

and where in the PWIA, the initial momentum  $\mathbf{p}_m$  would equal the experimental missing momentum  $\mathbf{p}_{\text{miss}}$ . Thus, the momentum distribution

$$\rho(p_m) = \frac{1}{2\pi^2} (|\tilde{f}_{\kappa}(p_m)|^2 + |\tilde{g}_{\kappa}(p_m)|^2) \quad (\text{A20})$$

is obtained, normalized to

$$4\pi \int dp p_m^2 \rho(p_m) = 1 \quad (\text{A21})$$

for unit occupancy.

Similarly, let

$$\Psi^{(+)}(\mathbf{p}, \mathbf{r}) = \sqrt{\frac{E+m}{2E}} \begin{pmatrix} \psi(\mathbf{r}) \\ \zeta(\mathbf{r}) \end{pmatrix} \quad (\text{A22})$$

represent a wave function of the  $N+B$  system with an incoming Coulomb wave and outgoing spherical waves open in all channels. Specific details regarding the boundary conditions may be found in Refs. [94,120,121].

The Madrid RDWIA calculations [16] employ a partial-wave expansion of the first-order Dirac equation, leading to a pair of coupled first-order differential equations. Alternatively, the LEA code [122] by Kelly uses the Numerov algorithm to solve a single second-order differential equation that emerges from an equivalent Schrödinger equation of the form

$$[\nabla^2 + k^2 - 2\mu(U^C + U^{LS}\mathbf{L} \cdot \boldsymbol{\sigma})]\xi = 0, \quad (\text{A23})$$

where  $k$  is the relativistic wave number,  $\mu$  is the reduced energy, and

$$U^C = \frac{E}{\mu} \left[ V + \frac{m}{E} S + \frac{S^2 - V^2}{2E} \right] + U^D, \quad (\text{A24a})$$

$$U^D = \frac{1}{2\mu} \left[ -\frac{1}{2r^2 D} \frac{d}{dr} (r^2 D') + \frac{3}{4} \left( \frac{D'}{D} \right)^2 \right], \quad (\text{A24b})$$

$$U^{LS} = -\frac{1}{2\mu} \frac{D'}{rD}, \quad (\text{A24c})$$

$$D = 1 + \frac{S-V}{E+m}. \quad (\text{A24d})$$

$S$  and  $V$ <sup>16</sup> are, respectively, the scalar and vector potential terms of the original four-component Dirac equation (see Ref. [2]).  $D(r)$  is known as the Darwin nonlocality factor and  $U^C$  and  $U^{LS}$  are the central and spin-orbit potentials. The Darwin potential  $U^D$  is generally quite small. The upper and

lower components of the Dirac wave function are then obtained using

$$\psi = D^{1/2} \xi, \quad (\text{A25a})$$

$$\zeta = \frac{\boldsymbol{\sigma} \cdot \mathbf{p} \psi}{E + m + S - V}. \quad (\text{A25b})$$

This method is known as direct Pauli reduction [18,79]. A very similar approach is also employed by Meucci *et al.* [81]. A somewhat similar approach based on the Eikonal Approximation (see the discussion of the ROMEA calculations in Appendix A 2) has been employed by Radici *et al.* [123,124].

For our purposes, the two most important differences between relativistic and nonrelativistic DWIA calculations are the suppression of the interior wave function by the Darwin factor in Eq. (A25a), and the dynamical enhancement of the lower components of the Dirac spinor (also known as “spinor distortion”) by the strong Dirac scalar and vector potentials in Eq. (A25b).

As demonstrated in Refs. [18,125,126], the Darwin factor tends to increase the normalization factors deduced using an RDWIA analysis. Distortion of the bound-nucleon spinor destroys factorization and at large  $p_{\text{miss}}$  produces important oscillatory signatures in the interference response functions,  $A_{LT}$ , and recoil polarization—see Refs. [19–21,94,127]. The effect of spinor distortion within the Effective Momentum Approximation (EMA) has been studied by Kelly [94]. The LEA code has subsequently been upgraded to evaluate Eq. (A25) without applying the EMA. These two methods for constructing the ejectile distorted waves should be equivalent. The predictions of the LEA and the Madrid codes given identical input are compared in Sec. IV A.

The approximations made by DWIA violate current conservation and introduce gauge ambiguities. The most common prescriptions,

$$\mathcal{J}_q \rightarrow \frac{\omega}{q} \mathcal{J}_0, \quad (\text{A26a})$$

$$\mathcal{J}_\mu \rightarrow \mathcal{J}_\mu + \frac{\mathcal{J} \cdot q}{Q^2} q_\mu, \quad (\text{A26b})$$

$$\mathcal{J}_0 \rightarrow \frac{q}{\omega} \mathcal{J}_q, \quad (\text{A26c})$$

correspond to Coulomb, Landau, and Weyl gauges, respectively. Typically, Gordon ambiguities and sensitivity to details of the off-shell extrapolation are largest in the Weyl gauge. Although there is no fundamental preference for any of these prescriptions, it appears that the data are in general least supportive of the Weyl gauge. Further, the CC1 operator is the most sensitive to spinor distortion while the CC3 operator is the least. The intermediate CC2 is chosen most often for RDWIA.

Besides the interaction in the final state of the outgoing proton, in any realistic calculation with finite nuclei, the effect of the distortion of the electron wave function must be taken into account. For relatively light nuclei and large ki-

<sup>16</sup>Note that the calculations in Ref. [2] using LEA neglected the  $(S-V)$  term and replaced the momentum in Eq. (A25b) by its asymptotic value, an approach later called EMA-noSV, where EMA denotes the Effective Momentum Approximation.

netic energies, the EMA for electron distortion (the “ $q_{\text{eff}}$  Approximation”) is sufficient—see Refs. [128,129]. In this approach, the electron current is approximated by

$$j^\mu(\mathbf{q}_{\text{eff}}) \approx \frac{\bar{k}_i \bar{k}_f}{k_i k_f} \bar{u}(\bar{\mathbf{k}}_f) \gamma^\mu u(\bar{\mathbf{k}}_i), \quad (\text{A27})$$

where  $\mathbf{q}_{\text{eff}} = \bar{\mathbf{k}}_i - \bar{\mathbf{k}}_f$  is the effective momentum transfer based upon the effective wave numbers

$$\bar{\mathbf{k}} = \mathbf{k} + f_Z \frac{\alpha Z}{R_Z} \hat{\mathbf{k}}, \quad (\text{A28})$$

with  $f_Z \approx 1.5$  and  $R_Z \approx 1.2A^{1/3}$ . For all the RDWIA calculations presented in this paper that are compared directly with data, this “ $q_{\text{eff}}$  Approximation” has been used to account for electron Coulomb distortion. Only the RPWIA and RDWIA<sub>( $U^{\text{opt}}=0$ )</sub> comparison calculations shown in Fig. 7, the baseline RDWIA comparison calculations shown in Figs. 8 and 9, and the RDWIA and RMSGA comparison calculations shown in Fig. 10 omit the effect of electron Coulomb distortion. This is equivalent to setting  $f_Z=0$  in Eq. (A28).

## 2. ROMEA/RMSGA

The Eikonal Approximation (EA) belongs to the class of semi-classical approximations which are meant to become “exact” in the limit of small de Broglie ( $db$ ) wavelengths,  $\lambda_{db} \ll a$ , where  $a$  is the typical range of the potential in which the particle is moving. For a particle moving in a relativistic (optical) potential consisting of scalar and vector terms, the scattering wave function takes on the EA form

$$\psi_F(\mathbf{r}) \sim \left[ \frac{1}{E + m + S - V - \boldsymbol{\sigma} \cdot \mathbf{p}} \right] e^{i\mathbf{p} \cdot \mathbf{r}} e^{iS(\mathbf{r})} \chi_{m_s}. \quad (\text{A29})$$

This wave function differs from a relativistic plane wave in two respects: first, there is a dynamical relativistic effect from the scalar ( $S$ ) and vector ( $V$ ) potentials which enhances the contribution from the lower components; and second, the wave function contains an eikonal phase which is determined by integrating the central ( $U^C$ ) and spin-orbit ( $U^{LS}$ ) terms of the distorting potentials along the (asymptotic) trajectory of the escaping particle. In practice, this amounts to numerically calculating the integral [ $\mathbf{r} \equiv (\mathbf{b}, z)$ ]

$$iS(\mathbf{b}, z) = -i \frac{m}{K} \int_{-\infty}^z dz' [U^C(\mathbf{b}, z') + U^{LS}(\mathbf{b}, z')] \\ \times [\boldsymbol{\sigma} \cdot (\mathbf{b} \times \mathbf{K}) - iKz'], \quad (\text{A30})$$

where  $\mathbf{K} \equiv \frac{1}{2}(\mathbf{p} + \mathbf{q})$ . Within the ROMEA calculation, the eikonal phase given by Eq. (A30) is computed from the relativistic optical potentials as they are derived from global fits to elastic proton-nucleus scattering data. It is worth stressing that the sole difference between the ROMEA and the RDWIA models is the use of the EA to compute the scattering wave functions.

For proton lab momenta exceeding 1 GeV/ $c$ , the highly inelastic nature of the elementary nucleon-nucleon  $NN$  scat-

tering process makes the use of a potential method for describing FSI effects somewhat artificial. In this high-energy regime, an alternate description of FSI processes is provided by the Glauber Multiple-Scattering Theory. A relativistic and unfactorized formulation of this theory has been developed by the Ghent Group [87,88]. In this framework, the  $A$ -body wave function in the final state reads as

$$\Psi_A^{\mathbf{p}}(\mathbf{r}, \mathbf{r}_2, \mathbf{r}_3, \dots, \mathbf{r}_A) \sim \hat{\mathcal{O}} \left[ \frac{1}{E + m} \boldsymbol{\sigma} \cdot \mathbf{p} \right] e^{i\mathbf{p} \cdot \mathbf{r}} \chi_{m_s} \\ \times \Psi_B(\mathbf{r}_2, \dots, \mathbf{r}_A), \quad (\text{A31})$$

where  $\Psi_B$  is the wave function characterizing the state in which the  $B$  nucleus is created. In the above expression, the subsequent elastic or “mildly inelastic” collisions which the ejectile undergoes with “frozen” spectator nucleons are implemented through the introduction of the operator

$$\hat{\mathcal{O}}(\mathbf{r}, \mathbf{r}_2, \mathbf{r}_3, \dots, \mathbf{r}_A) \equiv \prod_{j=2}^A [1 - \Gamma(p, \mathbf{b} - \mathbf{b}_j) \theta(z - z_j)],$$

where the profile function for  $pN$  scattering is

$$\Gamma(p, \mathbf{b}) = \frac{\sigma_{pN}^{\text{tot}}(1 - i\epsilon_{pN})}{4\pi\beta_{pN}^2} \exp\left(-\frac{b^2}{2\beta_{pN}^2}\right).$$

In practice, for the lab momentum of a given ejectile, the following input is required: the total proton-proton and proton-neutron cross section  $\sigma_{pN}^{\text{tot}}$ , the slope parameter  $\beta_{pN}$ , and the ratio of the real-to-imaginary scattering amplitude  $\epsilon_{pN}$ . The parameters  $\sigma_{pN}^{\text{tot}}$ ,  $\beta_{pN}$ , and  $\epsilon_{pN}$  are obtained through interpolation of the data base made available by the Particle Data Group [130]. The  $A(e, e'N)B$  results obtained with a scattering state of the form of Eq. (A31) are referred to as RMSGA calculations. It is worth stressing that in contrast to the RDWIA and the ROMEA models, all parameters entering the calculation of the scattering states in RMSGA are directly obtained from the elementary proton-proton and proton-neutron scattering data. Thus, the scattering states are not subject to the  $SV$  effects discussed in Appendix A 1, which typically arise when relativistic potentials are employed. However, the  $SV$  effects are included for the bound-state wave function.

Note that for the kinematics of the  $^{16}\text{O}(e, e'p)$  experiment presented in this paper, the de Broglie wavelength of the ejected proton is  $\lambda_{db} \approx 1.3$  fm, and thus both the optical potential and the Glauber frameworks may be applicable. Indeed, for  $T_p \approx 0.433$  GeV, various sets of relativistic optical potentials are readily available and  $\lambda_{db}$  appears sufficiently small for the approximations entering the Glauber framework to be justifiable—see Ref. [87].

## APPENDIX B: A “DIP”-REGION INVESTIGATION

A small portion of the beam time allocated to the measurement discussed in the main body of this article was used for an exploratory investigation of the “dip” located in the energy-transfer region between the QE peak and the

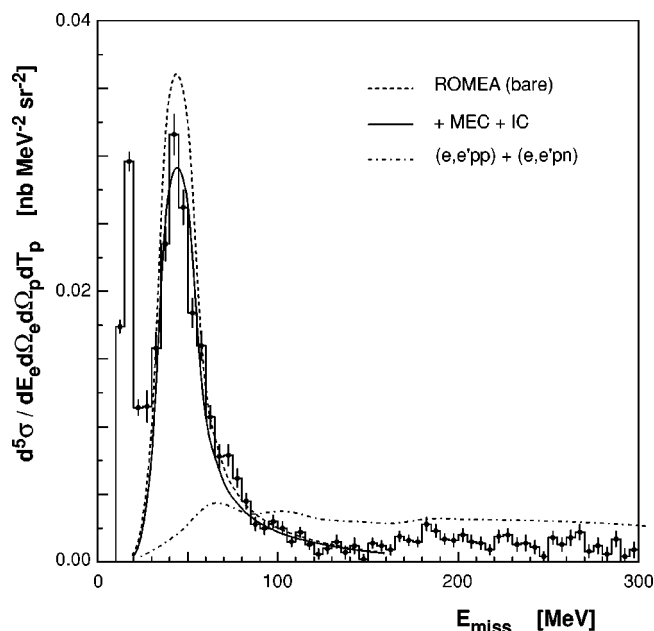


FIG. 25. Data from this work together with calculations by the Ghent Group for the  $E_{\text{miss}}$ -dependence of the cross-section data obtained in dip-region kinematics for  $E_{\text{beam}}=1.643$  GeV. Uncertainties are statistical and, on average, there is an additional  $\pm 5.9\%$  systematic uncertainty associated with the data.

$\Delta(1232)$ -resonance. For this investigation,  $E_{\text{beam}}=1.643$  GeV was employed, and the  $\text{HRS}_e$  position and central momentum were fixed at  $\theta_e=37.17^\circ$  and  $p_e=1056$  MeV/ $c$ , respectively. This resulted in  $q \approx 1.026$  GeV/ $c$ ,  $\omega \approx 589$  MeV,  $Q^2 \approx 0.706$  (GeV/ $c$ ) $^2$ , and

$y=0.16$ .<sup>17</sup> The  $\text{HRS}_h$  was then positioned at  $\theta_h=38.45^\circ$  ( $\theta_{pq}=0^\circ$ ) and its central momentum varied from 828 MeV/ $c$  to 1190 MeV/ $c$  in five steps of  $\Delta p_p \approx 70$  MeV/ $c$  per step. These momentum settings were close enough to each other that there was adequate acceptance overlap between them to allow for radiative corrections to be performed. The configuration of the experimental apparatus and data-acquisition system was identical in all aspects to that used for the QE measurement. The data analysis was also identical to that performed on the QE data, save for an additional cut to remove  $\text{H}(e, e'p)\pi^0$  events.

Figure 25 shows the measured cross-section data for the dip region as a function of  $E_{\text{miss}}$  compared to calculations by the Ghent Group for  $E_{\text{beam}}=1.643$  GeV. The dashed curve is the bare ROMEIA calculation for proton knockout from the  $1s_{1/2}$ -state of  $^{16}\text{O}$  and the solid curve is the same calculation including the effects of MEC and IC (see the main text of this article for further details). A normalization factor of 1.0 was employed for these calculations. The dashed-dotted curve illustrates the calculated  $(e, e'pN)$  contribution. In contrast to the QE energy region, the bare calculation actually overestimated the  $1s_{1/2}$ -state strength in these kinematics. Also in contrast to the QE energy region, the inclusion of MEC and IC decreased the magnitude of the calculated cross section and improved the agreement. Finally, while the  $(e, e'pN)$  calculations have the measured flat shape for  $E_{\text{miss}} > 100$  MeV, they are twice as large as the cross-section data.

<sup>17</sup>The quantity  $y$  (which is the minimum value of the initial momentum of the nucleon) is generally used to label non-QE kinematics. According to Day *et al.* [131],  $y = [(m_A + \omega)\sqrt{\Lambda^2 - m_B^2}W^2 - q\Lambda]/W^2$ , where  $W = \sqrt{(m_A + \omega)^2 - q^2}$  and  $\Lambda = (m_B^2 - m_N^2 + W^2)/2$ . In QE kinematics,  $y=0$ .

- [1] S. Frullani and J. Mougey, in *Advances in Nuclear Physics*, edited by J. W. Negel and E. Vogt (Plenum, New York, 1984), Vol. 14, p. 1, and references therein.
- [2] J. J. Kelly, *Adv. Nucl. Phys.* **23**, 75 (1996), and references therein.
- [3] S. Boffi, C. Giusti, F. D. Pacati, and M. Radici, *Electromagnetic Response of Atomic Nuclei* (Oxford University Press, Oxford, 1996).
- [4] J. J. Kelly, *Phys. Rev. C* **56**, 2672 (1997).
- [5] U. Amaldi *et al.*, *Phys. Lett.* **25B**, 24 (1967).
- [6] J. Mougey *et al.*, *Nucl. Phys.* **A262**, 461 (1976).
- [7] A. Picklesimer, J. W. Van Orden, and S. J. Wallace, *Phys. Rev. C* **32**, 1312 (1985).
- [8] A. Picklesimer and J. W. Van Orden, *Phys. Rev. C* **35**, 266 (1987).
- [9] A. Picklesimer and J. W. Van Orden, *Phys. Rev. C* **40**, 290 (1989).
- [10] H. Mütter and W. H. Dickhoff, *Phys. Rev. C* **49**, R17 (1994).
- [11] M. Bernheim *et al.*, *Nucl. Phys.* **A375**, 381 (1982).
- [12] L. Chinitz *et al.*, *Phys. Rev. Lett.* **67**, 568 (1991).
- [13] C. M. Spaltro *et al.*, *Phys. Rev. C* **48**, 2385 (1993).
- [14] M. Leuschner *et al.*, *Phys. Rev. C* **49**, 955 (1994).
- [15] K. I. Blomqvist *et al.*, *Phys. Lett. B* **344**, 85 (1995).
- [16] J. M. Udías, P. Sarriguren, E. Moya de Guerra, E. Garrido, and J. A. Caballero, *Phys. Rev. C* **48**, 2731 (1993).
- [17] E. Hummel and J. A. Tjon, *Phys. Rev. C* **49**, 21 (1994).
- [18] J. M. Udías, P. Sarriguren, E. Moya de Guerra, E. Garrido, and J. A. Caballero, *Phys. Rev. C* **51**, 3246 (1995).
- [19] J. A. Caballero, T. W. Donnelly, E. Moya de Guerra, and J. M. Udías, *Nucl. Phys.* **A643**, 189 (1998).
- [20] J. M. Udías, J. A. Caballero, E. Moya de Guerra, J. E. Amaro, and T. W. Donnelly, *Phys. Rev. Lett.* **83**, 5451 (1999).
- [21] J. M. Udías and J. R. Vignote, *Phys. Rev. C* **62**, 034302 (2000).
- [22] R. Lourie *et al.*, *Phys. Rev. Lett.* **56**, 2364 (1986).
- [23] P. E. Ulmer *et al.*, *Phys. Rev. Lett.* **59**, 2259 (1987).
- [24] L. B. Weinstein *et al.*, *Phys. Rev. Lett.* **64**, 1646 (1990).
- [25] M. Holtrop *et al.*, *Phys. Rev. C* **58**, 3205 (1998).
- [26] J. H. Morrison *et al.*, *Phys. Rev. C* **59**, 221 (1999).
- [27] J. B. J. M. Lanen *et al.*, *Phys. Rev. Lett.* **64**, 2250 (1990).
- [28] G. van der Steenhoven *et al.*, *Nucl. Phys.* **A480**, 547 (1988).
- [29] D. Dutta *et al.*, *Phys. Rev. C* **61**, 061602(R) (2000).
- [30] D. Dutta *et al.*, *Phys. Rev. C* **68**, 064603 (2003).
- [31] T. Takaki, *Phys. Rev. C* **39**, 359 (1989).



- [32] J. Ryckebusch *et al.*, Nucl. Phys. **A624**, 581 (1997).
- [33] A. Gil, J. Nieves, and E. Oset, Nucl. Phys. **A627**, 599 (1997).
- [34] A. Saha, W. Bertozzi, R. W. Lourie, and L. B. Weinstein, Experiment Proposal E89-003, Jefferson Laboratory, 1989; see also [http://www.jlab.org/exp\\_prog/experiments/summaries/](http://www.jlab.org/exp_prog/experiments/summaries/)
- [35] K. G. Fissum *et al.*, MIT-LNS Internal Report 2/97, Massachusetts Institute of Technology, 1997; see also <http://hallaweb.jlab.org/experiment/E89-003/e89003.html>
- [36] <http://hallaweb.jlab.org/>
- [37] <http://www.jlab.org/>
- [38] J. Alcorn *et al.*, Nucl. Instrum. Methods Phys. Res. A **522**, 294 (2004).
- [39] J. Gao *et al.*, MIT-LNS Internal Report 4/98, Massachusetts Institute of Technology, 1998; see also <http://hallaweb.jlab.org/experiment/E89-003/e89003/learned/e89003-beamdel.ps.gz>
- [40] *Hall A Operations Manual* (2001); see also <http://hallaweb.jlab.org/document/OPMAN/index.html>
- [41] K. B. Unser, IEEE Trans. Nucl. Sci. **28**, 2344 (1981).
- [42] P. E. Ulmer, Internal Report to the E89-003 Collaboration, Old Dominion University, 1998; see also <http://hallaweb.jlab.org/experiment/E89-003/e89003/learned/e89003-charge.ps.gz>
- [43] W. Barry *et al.*, Technical Memorandum JLAB-TN-90-246, Jefferson Laboratory, 1990.
- [44] W. Barry *et al.*, Technical Memorandum JLAB-TN-91-087, Jefferson Laboratory, 1991.
- [45] <http://www.aps.anl.gov/epics>.
- [46] C. K. Sinclair, Technical Memorandum JLAB-TN-92-064, Jefferson Laboratory, 1992.
- [47] F. Garibaldi *et al.*, Nucl. Instrum. Methods Phys. Res. A **314**, 1 (1992).
- [48] [http://hallaweb.jlab.org/equipment/high\\_resol.html](http://hallaweb.jlab.org/equipment/high_resol.html)
- [49] N. Liyanage *et al.*, MIT-LNS Internal Report 5/98, Massachusetts Institute of Technology, 1998; see also <http://hallaweb.jlab.org/experiment/E89-003/e89003/learned/e89003-optics.ps.gz>
- [50] M. Liang, Technical Memorandum JLAB-TN-99-029, Jefferson Laboratory, 1998; see also [http://hallaweb.jlab.org/experiment/E89-003/e89003/learned/survey\\_summary.ps.gz](http://hallaweb.jlab.org/experiment/E89-003/e89003/learned/survey_summary.ps.gz)
- [51] <http://hallaweb.jlab.org/equipment/detectors/detectors.html>; <http://hallaweb.jlab.org/equipment/detectors/trig.html>
- [52] K. G. Fissum *et al.*, Nucl. Instrum. Methods Phys. Res. A **474**, 108 (2001).
- [53] K. G. Fissum *et al.*, Technical Memorandum JLAB-TN-00-016, Jefferson Laboratory, 2000; see also <http://hallaweb.jlab.org/equipment/vdc/vdcs.html>
- [54] M. Iodice *et al.*, Nucl. Instrum. Methods Phys. Res. A **411**, 223 (1998); see also <http://hallaweb.jlab.org/equipment/detectors/gas.html>
- [55] <http://hallaweb.jlab.org/equipment/acquisition.html>
- [56] <http://coda.jlab.org/>
- [57] <http://hallaweb.jlab.org/equipment/daq/dplot.html>
- [58] <http://pierre.mit.edu/compserv/abacus/>
- [59] <http://hallaweb.jlab.org/espace/index.html>
- [60] J. Gao, Ph.D. thesis, Massachusetts Institute of Technology, 1999.
- [61] N. Liyanage, Ph.D. thesis, Massachusetts Institute of Technology, 1999.
- [62] R. Owens, Nucl. Instrum. Methods Phys. Res. A **288**, 574 (1990).
- [63] H. Baghaei, Ph.D. thesis, Massachusetts Institute of Technology, 1988.
- [64] G. G. Simon, C. Schmitt, F. Borkowski, and V. H. Walther, Nucl. Phys. **A333**, 381 (1980).
- [65] L. E. Price *et al.*, Phys. Rev. D **4**, 45 (1971).
- [66] [http://www.jlab.org/~mliang/deadtime\\_cor/](http://www.jlab.org/~mliang/deadtime_cor/)
- [67] E. Quint, Ph.D. thesis, University of Amsterdam, 1998.
- [68] R. Florizone, Ph.D. thesis, Massachusetts Institute of Technology, 1999.
- [69] E. Borie and D. Drechsel, Nucl. Phys. **A167**, 369 (1971).
- [70] J. A. Templon, C. E. Vellidis, R. E. J. Florizone, and A. J. Sarty, Phys. Rev. C **61**, 014607 (2000).
- [71] <http://www.physics.odu.edu/~ulmer/mceep/mceep.html>
- [72] A. S. Raskin and T. W. Donnelly, Ann. Phys. (N.Y.) **191**, 78 (1989).
- [73] M. N. Rosenbluth, Phys. Rev. **79**, 615 (1950).
- [74] K. G. Fissum and P. E. Ulmer, Technical Memorandum JLAB-TN-02-015, Jefferson Laboratory, 2002; see also [http://hallaweb.jlab.org/experiment/E89-003/e89003/learned/e89003\\_sysun\\_us.ps.gz](http://hallaweb.jlab.org/experiment/E89-003/e89003/learned/e89003_sysun_us.ps.gz)
- [75] M. Traini, S. Turck-Chièze, and A. Zghiche, Phys. Rev. C **38**, 2799 (1988).
- [76] J. M. Udías, Ph.D. thesis, Universidad Autonoma de Madrid, 1993.
- [77] J. P. McDermott, Phys. Rev. Lett. **65**, 1991 (1990).
- [78] Y. Jin, D. S. Onley, and L. E. Wright, Phys. Rev. C **45**, 1311 (1992).
- [79] M. Hedayati-Poor, J. I. Johansson, and H. S. Sherif, Phys. Rev. C **51**, 2044 (1995).
- [80] J. J. Kelly, Phys. Rev. C **60**, 044609 (1999).
- [81] A. Meucci, C. Giusti, and F. D. Pacati, Phys. Rev. C **64**, 014604 (2001).
- [82] J. J. Kelly, Internal Report to the E89-003 Collaboration, University of Maryland, 2003; see also <http://hallaweb.jlab.org/experiment/E89-003/e89003/publications/comparison.ps.gz>
- [83] M. M. Sharma, M. A. Nagarajan, and P. Ring, Phys. Lett. B **312**, 377 (1993).
- [84] E. D. Cooper, S. Hama, B. C. Clark, and R. L. Mercer, Phys. Rev. C **47**, 297 (1993).
- [85] D. Debruyne, J. Ryckebusch, W. Van Nespen, and S. Janssen, Phys. Rev. C **62**, 024611 (2000).
- [86] D. Debruyne and J. Ryckebusch, Nucl. Phys. **A699**, 65 (2002).
- [87] D. Debruyne, J. Ryckebusch, S. Janssen, and T. Van Caueren, Phys. Lett. B **527**, 67 (2002).
- [88] J. Ryckebusch, D. Debruyne, P. Lava, S. Janssen, B. Van Overmeire, and T. Van Caueren, Nucl. Phys. **A728**, 226 (2003); see also [nucl-th/0305066](http://nucl-th/0305066).
- [89] J. Ryckebusch and D. Debruyne, Internal Report to the E89-003 Collaboration, Ghent University, 2002; see also <http://hallaweb.jlab.org/experiment/E89-003/e89003/publications/gental.ps.gz>
- [90] R. J. Furnstahl, B. D. Serot, and H.-B. Tang, Nucl. Phys. **A615**, 441 (1997).
- [91] J. Gao *et al.*, Phys. Rev. Lett. **84**, 3265 (2000).
- [92] N. Liyanage *et al.*, Phys. Rev. Lett. **86**, 5670 (2001).
- [93] J. M. Udías and J. R. Vignote, Internal Report to the E89-003 Collaboration, Universidad Complutense de Madrid, 2001; see also <http://hallaweb.jlab.org/experiment/E89-003/e89003/publications/udvig89003f.ps.gz>
- [94] J. J. Kelly, Phys. Rev. C **59**, 3256 (1999).
- [95] C. Horowitz and B. Serot, Nucl. Phys. **A368**, 503 (1981).

- [96] C. J. Horowitz, D. P. Murdock, and B. D. Serot, *Computational Nuclear Physics* (Springer-Verlag, Berlin, 1991).
- [97] J. M. Udías *et al.*, Phys. Rev. C **64**, 024614 (2001); see also nucl-th/0101038.
- [98] J. A. McNeil, L. Ray, and S. J. Wallace, Phys. Rev. C **27**, 2123 (1983).
- [99] C. J. Horowitz, Phys. Rev. C **31**, 1340 (1985).
- [100] D. P. Murdock and C. J. Horowitz, Phys. Rev. C **35**, 1442 (1987).
- [101] M. Gari and W. Krümpelmann, Z. Phys. A **322**, 689 (1985).
- [102] D. H. Lu, A. W. Thomas, K. Tsushima, A. G. Williams, and K. Saito, Phys. Lett. B **417**, 217 (1998).
- [103] D. H. Lu, K. Tsushima, A. W. Thomas, A. G. Williams, and K. Saito, Phys. Rev. C **60**, 068201 (1999).
- [104] A. Saha, W. Bertozzi, L. B. Weinstein, and K. G. Fissum, Experiment Proposal E00-102, Jefferson Laboratory, 2000; see also [http://www.jlab.org/exp\\_prog/experiments/summaries/](http://www.jlab.org/exp_prog/experiments/summaries/) and <http://hallaweb.jlab.org/experiment/E00-102/e00102/e00102.html>
- [105] J. E. Amaro, A. M. Lallena, and J. A. Caballero, Phys. Rev. C **60**, 014602 (1999).
- [106] J. E. Amaro, M. B. Barbaro, J. A. Caballero, and F. Kazemi Tabatabaei, Phys. Rev. C **68**, 014604 (2003).
- [107] J. Ryckebusch, D. Debruyne, W. Van Nespén, and S. Janssen, Phys. Rev. C **60**, 034604 (1999).
- [108] J. Ryckebusch, K. Heyde, L. Machenil, D. Ryckbosch, M. Vanderhaeghen, and M. Waroquier, Phys. Rev. C **46**, R829 (1992).
- [109] S. Janssen *et al.*, Nucl. Phys. **A672**, 285 (2000).
- [110] J. J. Kelly, Internal Report to the E89-003 Collaboration, University of Maryland, 2002; see also <http://hallaweb.jlab.org/experiment/E89-003/e89003/publications/survey.ps.gz>
- [111] P. Mergell, U. G. Meißner, and D. Dreschsel, Nucl. Phys. **A596**, 367 (1996).
- [112] C. Barbieri and W. H. Dickhoff, Phys. Rev. C **65**, 064313 (2002).
- [113] L. Lapikás, G. van der Steenhoven, L. Frankfurt, M. Strikman, and M. Zhalov, Phys. Rev. C **61**, 064325 (2000).
- [114] K. I. Blomqvist *et al.*, Z. Phys. A **351**, 353 (1995).
- [115] L. Frankfurt, M. Strikman, and M. Zhalov, Phys. Lett. B **503**, 73 (2001).
- [116] J. A. Caballero, T. W. Donnelly, E. Moya de Guerra, and J. M. Udías, Nucl. Phys. **A632**, 323 (1998).
- [117] T. de Forest, Jr., Nucl. Phys. **A392**, 232 (1983).
- [118] C. R. Chinn and A. Picklesimer, Nuovo Cimento Soc. Ital. Fis., A **105**, 1149 (1992).
- [119] M. E. Rose, *Relativistic Electron Scattering* (Wiley, New York, 1961).
- [120] G. R. Satchler, *Direct Nuclear Reactions* (Oxford University Press, Oxford, 1983).
- [121] G. H. Rawitscher, Phys. Rev. C **56**, 2029 (1997).
- [122] J. J. Kelly, <http://www.physics.umd.edu/enp/jjkelly/LEA>
- [123] M. Radici, W. H. Dickhoff, and E. Roth Stoddard, Phys. Rev. C **66**, 014613 (2002).
- [124] M. Radici, A. Meucci, and W. H. Dickhoff, Eur. Phys. J. A **17**, 65 (2003).
- [125] S. Boffi, C. Giusti, and F. D. Pacati, Nuovo Cimento Soc. Ital. Fis., A **98**, 291 (1987).
- [126] Y. Jin and D. S. Onley, Phys. Rev. C **50**, 377 (1994).
- [127] M. C. Martínez, J. A. Caballero, and T. W. Donnelly, Nucl. Phys. A **707**, 83 (2002).
- [128] L. L. Schiff, Phys. Rev. **103**, 443 (1956).
- [129] C. Giusti and F. D. Pacati, Nucl. Phys. **A473**, 717 (1987).
- [130] Particle Data Group, K. Hagiwara *et al.*, Phys. Rev. D **66**, 010001 (2002).
- [131] D. B. Day *et al.*, Annu. Rev. Nucl. Part. Sci. **40**, 357 (1990).
- [132] See EPAPS Document No. E-PRVCAN-70-042407 for a complete archive of the data. A direct link to this document may be found in the online article's HTML reference section. The document may also be reached via the EPAPS homepage (<http://www.aip.org/pubservs/epaps.html>) or from <ftp.aip.org> in the directory/epaps/. See the EPAPS homepage for more information.